Dynamics and stability of water bells

By CHRISTOPHE CLANET

Institut de Recherche sur les Phénomènes Hors Equilibre, UMR 6594,
CNRS et Universités de Marseille I & II, Service 252, Campus de St. Jérôme,
13397 Marseille Cedex 20, France

The detailed experimental study conducted by Félix Savart in 1833 has revealed the existence of water bells when a cylindrical jet of diameter D_0 impacts with the velocity U_0 normally on to a disc of diameter D_i. We continue this study with a Newtonian fluid characterized by its density, ρ, kinematic viscosity, v, and surface tension, σ. We first show that for a given Reynolds number, $Re \equiv U_0 D_0 / v$, and Weber number, $We \equiv \rho U_0^2 D_0 / \sigma$, the domain where the bells exist in terms of the diameter ratio, $X \equiv D_i / D_0$, extends from the minimum value, X_-:

$$X_- = \frac{62}{We},$$

up to the maximum value, X_+:

$$17.6 \frac{X_+}{Re^{1/3}} \left[1 + 3.51 \left(\frac{X_+}{Re^{1/3}} \right)^3 \right] = \frac{We}{Re^{1/3}}.$$

In the domain, $X \in]X_-, X_+[$, the liquid film which results from the impact of the jet detaches at the edge of the disc, forming an angle ψ_0 with the direction of the jet. In the non-viscous limit, we show that this angle is determined by the nonlinear equation

$$\cos(\psi_0) - \cos(\psi_0^{max}) = \frac{8X}{We} \sin(\psi_0),$$

where ψ_0^{max} corresponds to the limit of ψ_0 for $We \gg 1$. In that limit, we find that $\cos(\psi_0^{max}) \approx 1 - 0.352 X^2$, for $X < 1$, and $\cos(\psi_0^{max}) \approx 0.1$ for $X > 1$.

The shape of the resulting bell is shown to be a catenary, first analytically described by Joseph Boussinesq in 1869. This shape results from the equilibrium between surface tension and centrifugal acceleration and is characterized by the length $L \equiv D_0 We / 16$. This solution holds in the low-gravity limit, $gL/U_0^2 \ll 1$, and when the pressure difference, p, across the liquid sheet is small, $pL/(2\sigma) \ll 1$. Considering the dynamics of formation of that catenary, we show that it is characterized by a quasi-constant velocity along the jet axis.

Finally, we show that these bells are not always stationary and may even undergo self-sustained oscillations. Studying their stability, we derive a general stability criterion and show the sensitivity of the bells to both the pressure difference across the liquid sheet and to the ejection angle. In this latter case, we find a critical angle of ejection above which the bell is periodically destroyed and created. The period of the cycle is shown to scale linearly with the formation time of the bell.

1. Introduction

In Paris in 1530, François I, King of France since 1515, decided at the request of his *maître de librairie*, Guillaume Budé, to create the institution *Le Collège Royal*, independent of the University of Paris, with the motto 'DOCET OMNIA': *It teaches everything*. The lectures were free, open to everybody and given by the best professors (Lecteurs) in the country. This institution became *Le Collège de France* in 1870. Felix Savart begun to teach there in 1828 and was given the chair of 'Physique Générale et Expérimentale' in 1836, following André-Marie Ampére. He died five years later on March 18, 1841, at 50 years of age.

The funeral speech, given by his friend A. C. Becquerel, sheds some light on the scientific approach of Savart: following his deep study of acoustics and electricity, he wanted to lay the foundations for molecular physics. To this end, Savart started to consider liquid jets as a flux of molecules, the size and the velocity of which can easily be controlled, and the structure of which can be studied through their response to an external forcing. This idea is set out by Savart in the introduction of his second out of four papers dedicated to liquid jets:

> Little attention has been paid so far to the phenomena involved in the impact of a liquid jet on a solid surface with which it forms a defined angle: the modifications introduced in the shape and in the state of the jet, as well as in the motion of the molecules after the impact, are still completely unknown, even in the simplest case one can imagine. However, it was easy to foresee that the study of such phenomena could shed light on some peculiarities of jets, and even on the properties of the liquids themselves.

The four papers published in 1833 deal with the general problem presented in figure 1(*a*). A cylindrical water jet of diameter $D_0[L]$,† impacts with the velocity $U_0[LT^{-1}]$, normally onto a disc of diameter $D_i[L]$. The Newtonian liquid being defined by its density $\rho[ML^{-3}]$, kinematic viscosity $v[L^2T^{-1}]$ and surface tension $\sigma[MT^{-2}]$, for similarity purposes, we characterize the initial fluid state with the non-dimensional Reynolds, $Re \equiv U_0D_0/v$, and Weber, $We \equiv \rho U_0^2 D_0/\sigma$, numbers that respectively compare inertia to viscosity and surface tension. Depending on the geometrical diameter ratio $X \equiv D_i/D_0$, several scenarios can be observed:

The singular limit $X = 0$, illustrated in figure 1(*b*), was the subject of the first paper Savart (1833*a*) and revealed the capillary instability of cylindrical liquid jets that was treated later by Plateau (1873) and Lord Rayleigh (1879).

The opposite limit $X \gg 1$, leads to the so-called hydraulic jump phenomenon, where a thick and quiescent layer of fluid is connected to the jet through a thin and rapid layer as presented in figure 1(*d*). The size of this stationary connecting region critically depends on both the injection parameters and the limit conditions at infinity Savart (1833*b*), Watson (1964).

In the intermediate domain $X \sim 1$, the liquid film is ejected from the impactor with the angle ψ_0 and Savart has shown that one can observe symmetrical water bells such as the one presented in figure 1(*c*).

Water bells and hydraulic jumps were together described in the second and third papers Savart (1833*b, c*) while the fourth (Savart 1833*d*) considered the impact of two facing jets.

Among all the observations and questions addressed by Savart in these papers, we concentrate here on the water bell problem. Following in Savart's footsteps, several

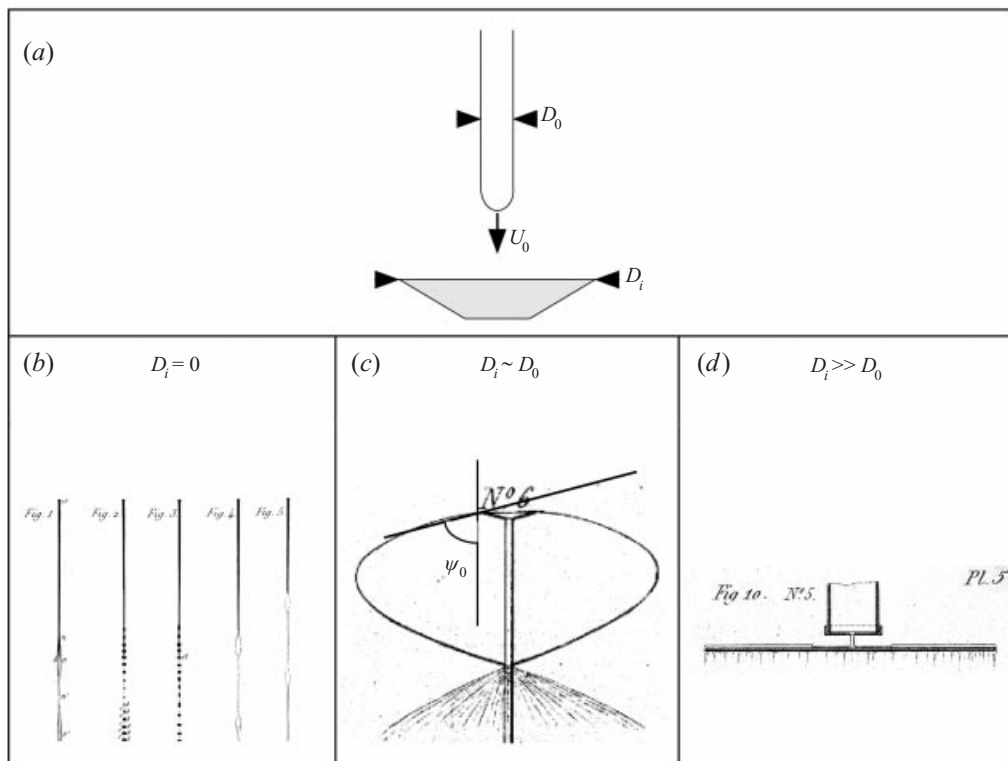† Terms in brackets indicate the dimension of the parameter: [*L*] length, [*T*] time, [*M*] mass.

FIGURE 1. Presentation of the problem addressed by Felix Savart: (*a*) sketch of the experiment; (*b*) capillary water jet instability from Savart (1833), Pl2, $D_0 = 6\,\text{mm}$, $Re = 9000$ and $We = 200$; (*c*) water bell from Savart (1833), $Pl6 - Fig14 - N°6$, $D_i/D_0 = 9$, $Re = 16300$ and $We = 1277$; (*d*) hydraulic jump from Savart (1833), $Pl5 - Fig10 - N°5$, $D_i/D_0 = 117$, $Re = 14320$ and $We = 626$.

studies have already been devoted to this subject, starting with two theoretical papers by Joseph Boussinesq in 1869 that give the general equations of the stationary bell shape, resulting from the equilibrium of several effects: surface tension, gravity, and inertia. In the limit where gravity is small compared to the two other contributions (surface tension and inertia), Boussinesq shows that the bell shape reduces to a catenary. Recently, Benedetto & Caglioti (1998) have deduced the catenary solution of Boussinesq from a stationary action principle. Experimentally, Bond (1935) used liquid bells to measure surface tension under dynamical conditions, and Hopwood (1952) described some remarkable shapes obtained when there is a difference of pressure between the inside and the outside of the bell. Shapes of bells were also studied theoretically by Lance & Perry (1953) and Taylor (1959) neglecting the motion of air inside the bell. Air motion was further studied by Parlange (1967). The extension of these studies to the case of swirling water bells was done by Bark *et al.* (1979), showing that in certain circumstances, the shape of a bell can be periodic along the axis of rotation.

Despite all the studies already devoted to water bells, several questions remain open concerning the criterion of detachment of the film from the impactor, the angle of ejection of the film, the dynamics of formation of the bell and its stability. These questions are addressed in the present paper in the low gravity limit, that is for ejection diameters D_0 not too large compared to the capillary length $a \equiv \sqrt{2\sigma/(\rho g)}$, where $g[LT^{-2}]$ is the acceleration due to gravity. Defining the Bond number as the
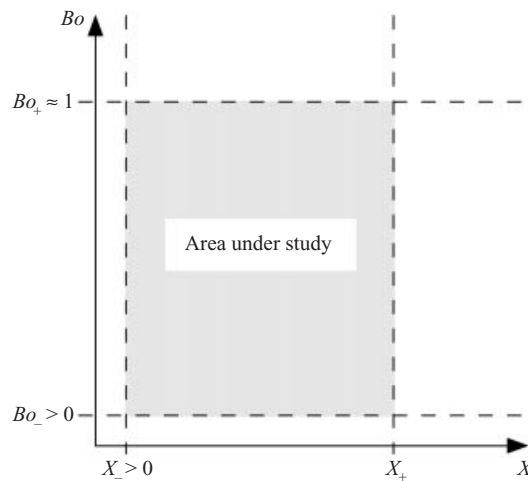
FIGURE 2. Domain of investigation in the parameter space (Bo, X).

ratio $Bo \equiv D_0/a$, the domain in which our study is conducted is shown shaded in figure 2, in the parameter space (Bo, X).

The singular limit $(X = 0, Bo = 0)$ that does not lead to a water bell is outside the scope of this study. If the diameter ratio X gets too large, $X > X_+$, one observes, instead of a bell, a hydraulic jump on the disc and the trickling of water at the edges. The bell regime is thus confined in the domain $X \in]X_-, X_+[$. If gravity effects dominate surface tension effects, the shape of the liquid sheet would result from an equilibrium between inertia and gravity and one would expect to observe a paraboloid of revolution instead of a bell. In this paper, we focus on the opposite limit where gravity effects can be neglected in comparison to capillary effects and we will show that this condition is fulfilled when $Bo \leqslant 1$.

Finally, throughout, the effect of the surrounding air is neglected. According to Squire (1953) and Huang (1970), this assumption is satisfied for moderate Weber numbers, $We < 1000$.

Section 2 describes the experimental setup used to produce and study the water bells. The experimental results and the models are respectively presented in §3 and §4, prior to the conclusions in §5.

2. Experimental setup

The general setup is presented in figure 3(a). Distilled water of density, $\rho = 1000 \, \text{kg m}^{-3}$, surface tension, $\sigma = 0.073 \, \text{kg s}^{-2}$, and kinematic viscosity, $\nu = 10^{-6} \text{m}^2 \, \text{s}^{-1}$, is initially contained in a pressurised reservoir. At the reservoir exit, two flow meters AALBORG, in a parallel setup allow the control of the flow from $0.2 \, \text{cm}^3 \, \text{s}^{-1}$ to $70 \, \text{cm}^3 \, \text{s}^{-1}$ with a graduation resolution of $0.2 \, \text{cm}^3 \, \text{s}^{-1}$. This enables an accurate control of the jet velocity U_0, defined as the ratio of the flow rate to the exit section area. Since the Froude number, $Fr_h = gh/U_0^2$, based the distance, h, from the nozzle to the impactor never exceeded 10^{-2}, the contraction and acceleration of the jet prior to the impact is neglected throughout.

The geometrical properties of the remaining two control parameters, D_0 and D_i, are presented in table 1. Three different nozzles are used to vary D_0 from 0.8 mm to 6.0 mm. The 0.8 mm jet is obtained with a thin hole in the wall of diameter, $D = 1$ mm, which leads to an effective jet diameter $D_0 \simeq 0.8D$; the theoretical derivation of the

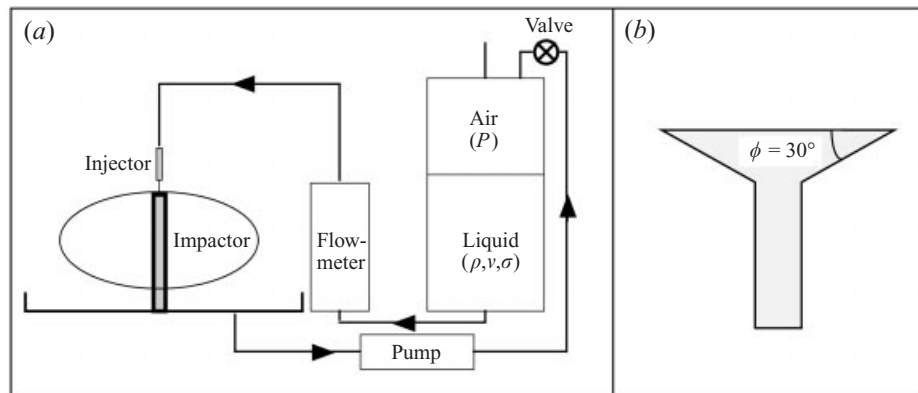FIGURE 3. Presentation of the experimental set-up: (*a*) general view, (*b*) detail of the impactor.

D_0 (mm)	0.8	3.0	6.0					
D_i (mm) $\begin{cases} \\ \end{cases}$	1.18	1.6	2.0	2.4	3.0	4.0	5.44	7.33
	9.87	13.3	17.91	24.13	32.51	43.79	58.99	107.4

TABLE 1. Geometrical properties of the jet diameter, D_0, and of the impactor diameter, D_i.

contraction coefficient for thin holes $D_0/D = \sqrt{\pi/(\pi + 2)}$ can be found in Landau & Lifchitz (1971). The 3 mm and 6 mm jets are created with a conical contraction, 25 mm long and 20 mm wide at the base. This leads to a contraction factor in cross-sectional area of 44 and 11 respectively, which ensures a quasi-top-hat velocity profile and a laminar jet up to Reynolds numbers of the order of $Re \approx 30\,000$.

The general shape of the impactor is presented in figure 3(*b*). Machined in aluminium, these impactors all have sharp edges with a carefully prepared upper surface. Their diameters range from 1.18 mm to 107.4 mm in the quasi-geometrical progression presented in table 1.

The apparatus is a closed loop to always use the same fluid and keep its characteristics constant. When the reservoir is almost empty, the experiment is stopped and the reservoir is filled up via a peristaltic pump.

Several results from Savart will be used and discussed in the present paper. For this reason, the experimental setup he used to produce water bells is presented in figure 4. A 4.44 m long tube TT′, of diameter 54 mm connects the constant-level reservoir B to the hole in T′ via the valve P. The exit velocity is measured through the pressure which is controlled in EE′E″. The exit hole of size D, is a thin hole in the wall shown in figure 4 (*Fig.* 4), which leads to an effective jet diameter $D_0 \simeq 0.8D$. The impactor in brass is shown in figure 4 (*Fig.* 3) with sharp edges and a carefully polished upper surface.

3. Experimental results

The presentation of our experimental results starts with a qualitative description of the influence of the control parameters, D_i, U_0 and D_0. This overview is completed with a quantitative second stage in which the results are collected in five subsections, concerning the detachment of the film from the impactor, the angle of ejection, the shape of the bells, the dynamics of their formation, and finally their stability.
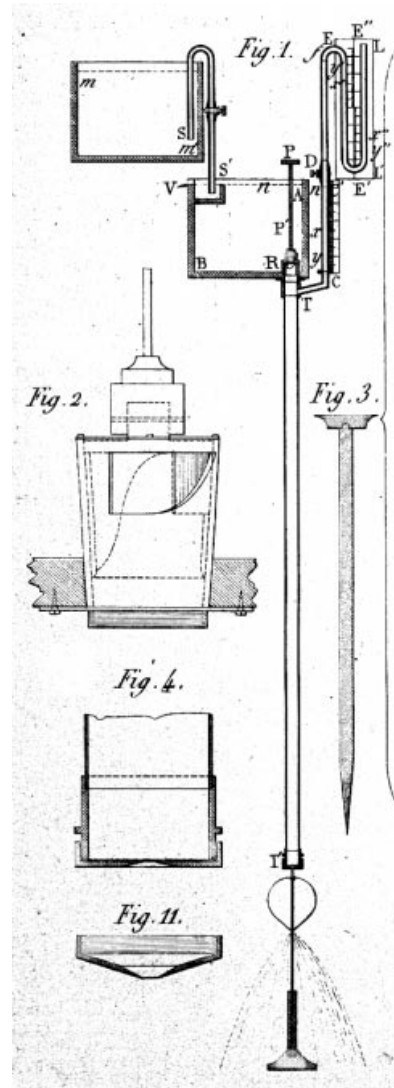
FIGURE 4. Experimental setup used by Savart (from Planche 4 of Savart's 1833 papers).

3.1. *A qualitative overview*

Figure 5 presents, for a fixed diameter, $D_0 = 3$ mm, and a fixed velocity, $U_0 = 2.08$ m s^{-1}, the influence of the impact diameter D_i. Under these conditions, Reynolds and Weber numbers are kept constant, $Re = 6240$, $We = 178$, and only $X \equiv D_i/D_0$ is varied. This set of experiments is conducted in the following way: the water jet is established and controlled at the beginning of the experiment without any impactor. The first impactor is then introduced on the axis of the jet. To avoid any hysteresis effect and to ensure that all the tests have the same initial conditions, we use a strong air jet to deviate the water jet from the impactor. The air jet is then removed and the stationary solution of the impact observed. This procedure is repeated several times to ensure that the observed solution is stable. The impactor is then replaced without touching the liquid jet and the whole procedure repeated with a new disc.
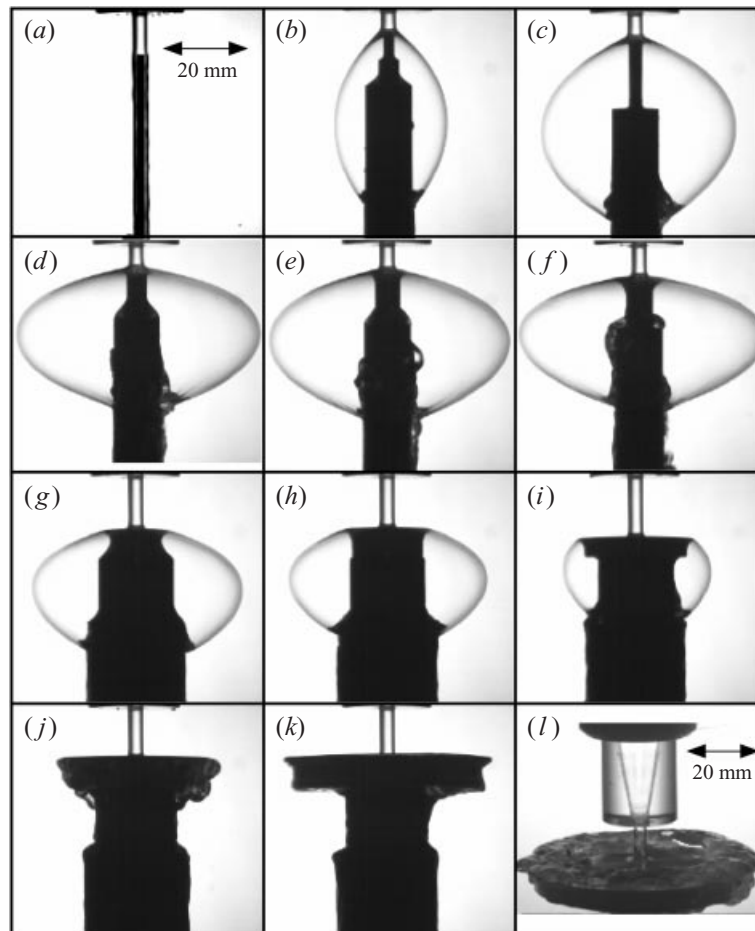
FIGURE 5. Influence of the impact diameter, D_i, for $D_0 = 3\,\text{mm}$, $U_0 = 2.08\,\text{m\,s}^{-1}$, $Re = 6240$, $We = 178$: (a) $D_i = 1.18\,\text{mm}$, (b) $3.0\,\text{mm}$, (c) $4.0\,\text{mm}$, (d) $5.44\,\text{mm}$, (e) $7.33\,\text{mm}$, (f) $9.87\,\text{mm}$, (g) $13.3\,\text{mm}$, (h) $17.81\,\text{mm}$, (i) $24.13\,\text{mm}$, (j) $32.51\,\text{mm}$, (k) $43.79\,\text{mm}$, (l) $58.99\,\text{mm}$.

From (a) to (l) the impactor diameter is progressively increased from $D_i = 1.18\,\text{mm}$ to $D_i = 58.99\,\text{mm}$. The spatial scale is kept the same from (a) to (k) and slightly reduced in (l), as indicated by the double arrow. For the smallest impactor (a), we observe that the water jet does not detach but rather surrounds the whole impactor and flows along its sides. Increasing the impact diameter, one reaches the critical value X_-, presented in figure 2, above which the film detaches at the edge of the impactor. Clearly, (b), obtained with $X = 1$, is above X_-. The liquid film is ejected from the impactor with a non-zero angle ψ_0 and exhibits a symmetrical shape about the equator plane, defined as the location of the maximal extension points. From (b) to (f), as the impact diameter becomes larger, the angle of ejection ψ_0 increases. This monotonic evolution stops between (f) and (g) and is replaced by the opposite tendency where ψ_0 decreases as D_i increases. This new behaviour continues up to (j) where the liquid film remains attached to the impactor. At this point, the critical diameter ratio X_+, is passed and we deduce that for these conditions, $8.04 < X_+ < 10.84$. In (j) and (k), the liquid film runs down the impactor without any detachment or hydraulic jump.
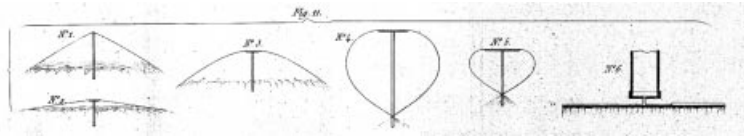
FIGURE 6. Figure 11 of Savart Planche 5: $D_0 = 4.7$ mm, $U_0 = 5.5$ m s^{-1}, $Re = 25850$, $We = 2031$ and N°1: $D_i = 0.65$ cm, N°2: $D_i = 4.05$ cm, N°3: $D_i = 5.40$ cm, N°4: $D_i = 10.80$ cm, N°5: $D_i = 16.30$ cm, N°6: $D_i = 55.00$ cm.
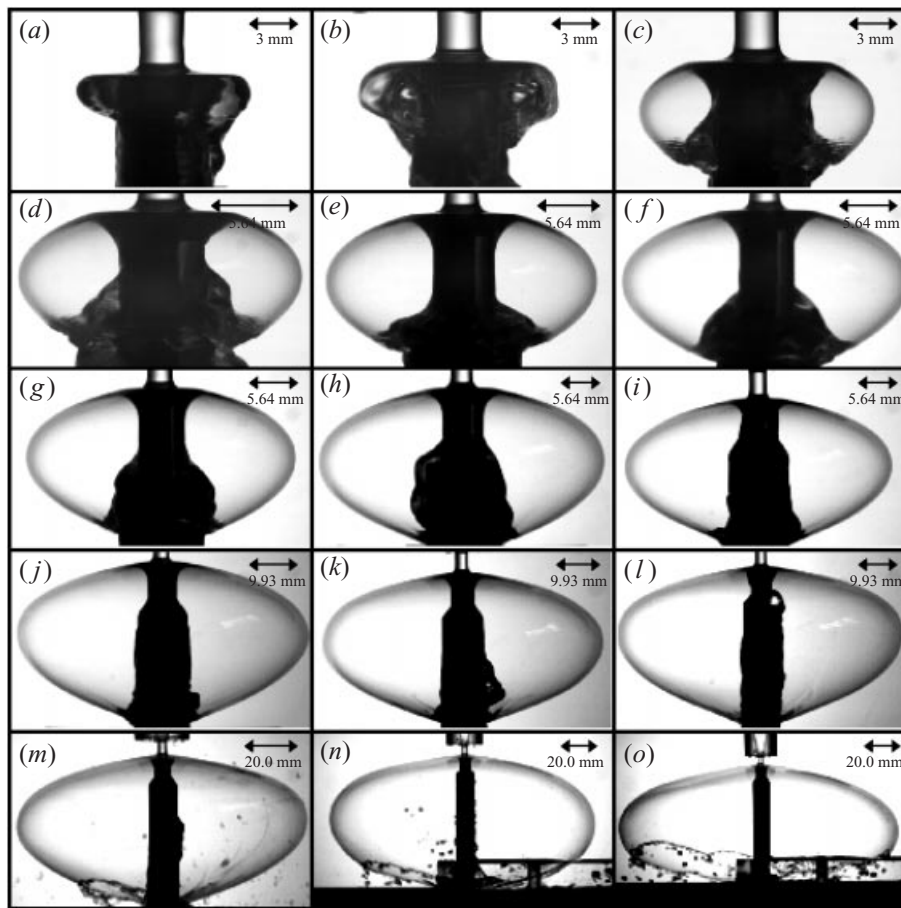

FIGURE 7. Influence of the impact velocity U_0 for $D_0 = 3$ mm, $D_i = 9.87$ mm: (*a*) $U_0 = 0.63$ m s^{-1}, (*b*) 1.0 m s^{-1}, (*c*) 1.08 m s^{-1}, (*d*) 1.2 m s^{-1}, (*e*) 1.42 m s^{-1}, (*f*) 1.57 m s^{-1}, (*g*) 1.68 m s^{-1}, (*h*) 1.87 m s^{-1}, (*i*) 2.08 m s^{-1}, (*j*) 2.25 m s^{-1}, (*k*) 2.42 m s^{-1}, (*l*) 2.65 m s^{-1}, (*m*) 2.88 m s^{-1}, (*n*) 3.43 m s^{-1}, (*o*) 3.67 m s^{-1}.

With the set of impactors used, the hydraulic jump on the impactor is first observed for $X = 19.7$ and presented in (*l*).

Some observations of Savart on the influence of the impactor diameter are reported in figure 6. These results were obtained, keeping $U_0 = 5.5$ m s^{-1} and $D_0 = 4.7$ mm, and increasing, from left to right, the diameter ratio X from 0.84 to 5.3, 7, 14, 21 and 72. This variation lead from open bells (N°1, 2 and 3) to closed bells (N°4 and 5) and then from closed bells to the hydraulic jump (N°6).

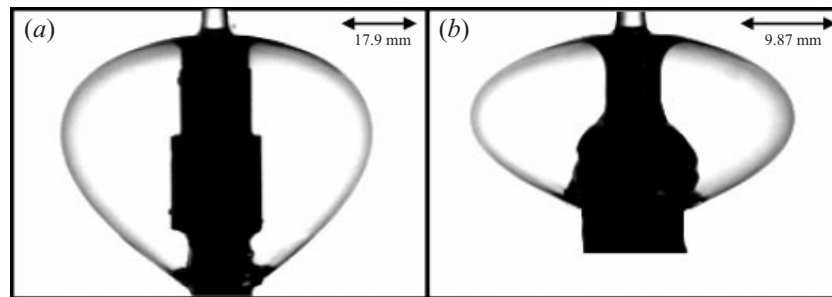To consider the influence of the jet velocity U_0, figure 7 presents for the fixed jet

FIGURE 8. Influence of the jet diameter D_0: (a) $D_0 = 6\,\text{mm}$, $D_i = 17.91\,\text{mm}$, $U_0 = 1.19\,\text{m s}^{-1}$, $\psi_0 = 73.8°$, $X = 2.985$, $We = 116$ and $Re = 7140$; (b) $D_0 = 3\,\text{mm}$, $D_i = 9.87\,\text{mm}$, $U_0 = 1.68\,\text{m s}^{-1}$, $\psi_0 = 72.2°$, $X = 3.29$, $We = 116$ and $Re = 5040$.

diameter, $D_0 = 3\,\text{mm}$, and the fixed impactor diameter, $D_i = 9.87\,\text{mm}$ ($X = 3.3$), the evolution of the liquid spreading when the velocity U_0 is increased from 0.63 to $3.67\,\text{m s}^{-1}$, from (a) to (o). We use the air jet procedure described above to check the stability of the solution presented. In this figure, the scale of each picture is adapted to the observed phenomenon. Figure 7 reveals that at low velocities, (a, b), the liquid spreads over the impactor and does not detach from it. A closer observation of (b) indicates that air bubbles start to be trapped in the streaming liquid. In (c), the film detaches and forms the first bell, characterized by a small angle of ejection ψ_0 and a symmetrical shape about the equatorial plane. This symmetry is not affected by the velocity and can be observed from (c) to (n). The angle of ejection ψ_0 first increases rapidly with the velocity from 60.6° in (c) to 70° in (e). This monotonic evolution continues but with a slower rate from (e) to (o) where ψ_0 reaches 81.2°. In this second domain, where the angle does not depend strongly on the velocity, the liquid bells we observe do not exhibit strong differences from one to the other. From (c) to (l), all the bells are closed. The last three pictures (m–o) exhibit holes in the liquid sheet around the closing point. The size of these holes increases with the velocity.

The influence of the jet diameter D_0, is presented in figure 8: (a) shows a closed bell obtained with the 6 mm injector whereas (b) was taken with the 3 mm injector. To illustrate the effect of the jet diameter only, we have kept constant the ratio, $X \simeq 3$, and the Weber number, $We = 116$. Both pictures have been rescaled so as to appear with the same jet diameter. The comparison of (a) with (b) reveals that the angle of ejection ψ_0 remains almost constant, $\psi_0 = 73.8°$ in (a) and $\psi_0 = 72.2°$ in (b) whereas the symmetry about the equatorial plane is broken for the 6 mm jet, the equatorial plane being closer to the impactor than to the closing point.

Some of Savart's observations on the influence of D_0 are reported in figure 9, where from (a) to (f), the jet diameter is decreased from 14.4 mm to 2.4 mm. In these experiments, the impact diameter is kept constant, $D_i = 27\,\text{mm}$, and the velocity adjusted so as to get the largest closed bell. From figure 9, we notice that the smaller the jet diameter, the closer we get to a symmetrical shape.

3.2. *On the detachment of the film from the impactor*

The formation of a water bell depends on the detachment of the film from the impactor, as illustrated in figures 5 and 7. Figure 5 indicates that for a given jet diameter and velocity, two limits in terms of the diameter ratio X, can be identified, X_- and X_+, outside which the liquid film remains attached to the impactor. In the case of a fixed jet diameter and diameter ratio, figure 7 shows that bells can only be observed
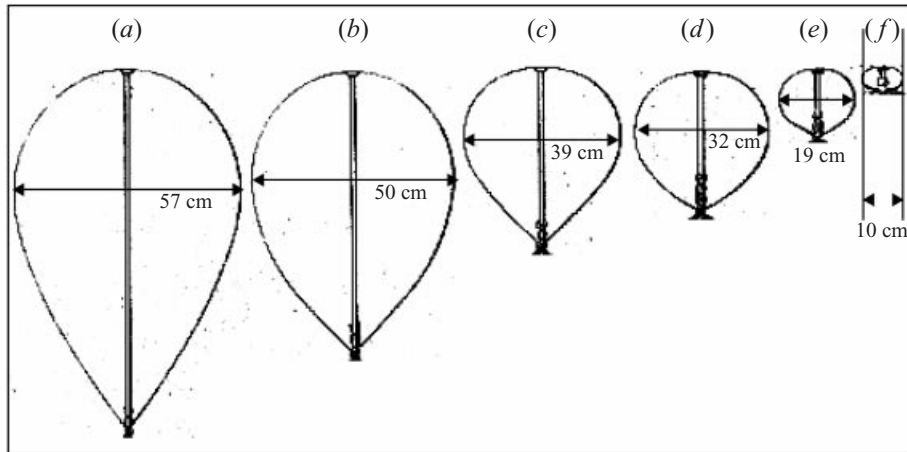
FIGURE 9. Savart's observations of the influence of the jet diameter: (a) $D_0 = 14.4$ mm, $U_0 = 2.06$ m s^{-1}, (b) $D_0 = 12$ mm, $U_0 = 2.15$ m s^{-1}, (c) $D_0 = 9.6$ mm, $U_0 = 2.54$ m s^{-1}, (d) $D_0 = 7.2$ mm, $U_0 = 2.67$ m s^{-1}, (e) $D_0 = 4.8$ mm, $U_0 = 3.16$ m s^{-1}, (f) $D_0 = 2.4$ mm, $U_0 = 5.66$ m s^{-1}.
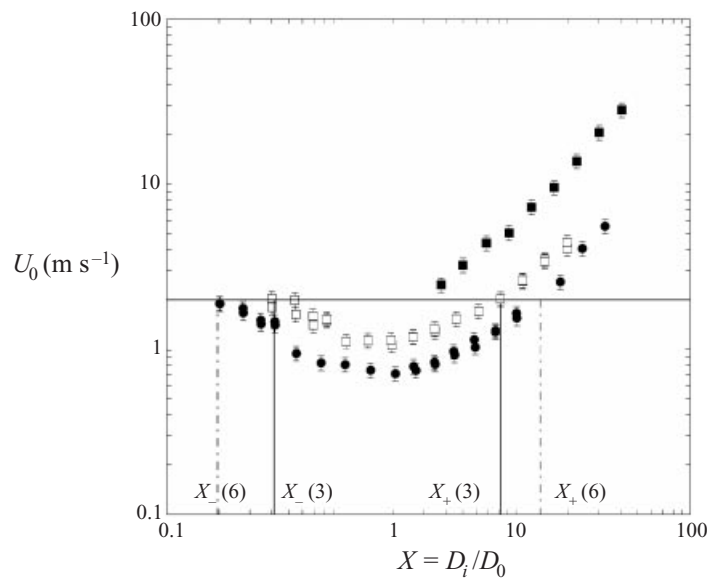

FIGURE 10. Evolution of the critical velocity of detachment U_0, with the diameter ratio $X = D_i/D_0$ (10% error bars): ■, $D_0 = 0.8$ mm; □, $D_0 = 3.0$ mm; ●, $D_0 = 6.0$ mm.

above a critical velocity. The function $U_0(X)$, between this critical velocity and the diameter ratio is presented in figure 10 for the three different jets diameters, 0.8 mm, 3.0 mm and 6.0 mm. All the points presented in figure 10 are obtained with the set of diameters presented in table 1 and through the same experimental procedure: for a given jet and impactor diameter, the velocity is progressively increased until the liquid film detaches from the impactor. To avoid any hysteresis effect, we use, after each velocity increase, the strong air jet procedure previously described. The whole procedure is then repeated with a different diameter ratio, and with the different jet diameters. With this procedure, the experimental uncertainty lies in the velocity, and the repeatability of the experiments indicates that this uncertainty is of the order of 10%.
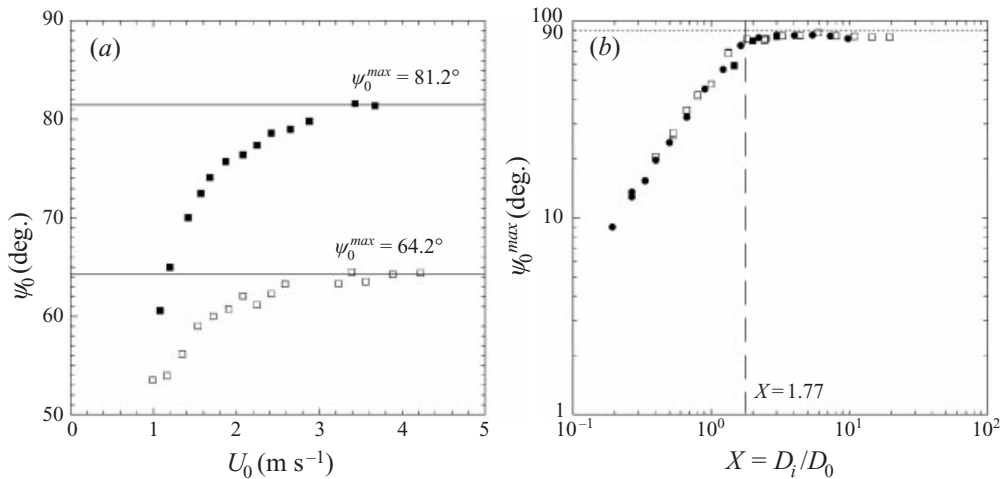
FIGURE 11. Evolution of the angle of ejection ψ_0: (*a*) with the velocity U_0 (■, $D_0 = 3$ mm and $D_i = 9.87$ mm; □, $D_0 = 3$ mm and $D_i = 4$ mm); (*b*) with the diameter ratio and large velocity (■, $D_0 = 0.8$ mm; □, $D_0 = 3.0$ mm; ●, $D_0 = 6.0$ mm).

We first concentrate on the function $U_0(X)$ obtained with $D_0 = 6$ mm, which is shown with black circles in figure 10: this function presents a minimum $U_0 \approx 0.71$ m s^{-1} for $X = X_c \approx 1.5$. For $D_0 = 6$ mm, no water bell can thus be observed below that velocity, whatever the diameter ratio, X. Above that critical velocity, the water bell region extends between the two intersections of the function $U_0(X)$ with the horizontal line $U_0 > U_0(X_c)$. For $U_0 = 2$ m s^{-1}, the two intersections $X_-(6) \approx 0.2$ and $X_+(6) \approx 13.8$ are shown in figure 10.

The function $U_0(X)$ obtained with $D_0 = 3$ mm (open squares) is similar to the one just described. The critical value X_c is found to be of the order of 1.5 and the corresponding velocity $U_0(1.5) \approx 1.05$ m s^{-1}. For a given diameter ratio X, the critical velocity for which the film detaches is always larger for $D_0 = 3$ mm than for $D_0 = 6$ mm. This behaviour implies that for a given velocity $U_0 = 2$ m s$^{-1} > U_0(X_c)$, the water bell region is always smaller for $D_0 = 3$ mm than for $D_0 = 6$ mm. According to figure 10 this region extends from $X_-(3) \approx 0.41$ up to $X_+(3) \approx 8$.

The function $U_0(X)$ obtained with $D_0 = 0.8$ mm (black squares), only exhibits an increasing behaviour with X, but we were not able with our set of diameters to investigate the region $X \leqslant 1$. However, this function confirms that for a given diameter ratio X, the critical velocity for which the film detaches increases as D_0 is decreased. For $X = 10$, we measure $U_0(6) = 1.6$ m s^{-1}, $U_0(3) = 2.4$ m s^{-1} and $U_0(0.8) = 5.8$ m s^{-1}.

3.3. *The angle of ejection* ψ_0

When the film detaches from the impactor, it makes an angle ψ_0 with the axis of the jet. For a given jet diameter, the sensitivity of this angle to both the diameter ratio X, and the velocity U_0, has been highlighted in figures 5 and 7.

The evolution of $\psi_0(U_0)$ corresponding to figure 7 is presented in figure 11(*a*) as black squares. Starting with a small value $\psi_0 = 60.6°$ close to the critical velocity of ejection, the angle increases with the velocity up to a maximal angle $\psi_0^{max} \approx 81.2°$. The function $\psi_0(U_0)$ is nonlinear, it increases strongly close to the critical velocity, for $1 < U_0 < 2$ m s^{-1}, and relaxes to ψ_0^{max} for $U_0 > 2$ m s^{-1}.

On figure 11(*a*), we also present the function $\psi_0(U_0)$ obtained with $D_0 = 3$ mm and

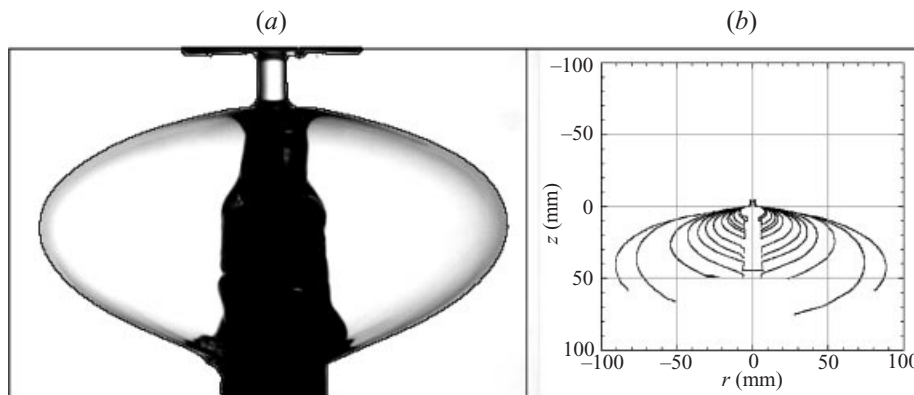(*a*)   (*b*)

FIGURE 12. Variation of the shape of the bell with U_0 for $D_0 = 3.0$ mm and $D_i = 9.87$ mm. (*a*) An example of the threshold method used to extract the bell shape for $U_0 = 2.08$ m s^{-1}. (*b*) evolution of the bell profile for decreasing velocities (in m s^{-1}): 3.67, 3.43, 2.88, 2.65, 2.42, 2.25, 2.08, 1.87, 1.68, 1.57, 1.42, 1.2, 1.08.

$D_i = 4$ mm. The evolution is similar to the one just described, but the maximal angle is lower, $\psi_0^{max} = 64.2°$.

The function $\psi_0^{max}(X)$ is presented in figure 11(*b*) for the three diameters $D_0 = 0.8$ mm, $D_0 = 3.0$ mm and $D_0 = 6.0$ mm. This figure reveals that ψ_0^{max} is a function only of X; it increases linearly with X in the range $X < 1.77$ and saturates at $84°$–$85°$ for $X > 1.77$.

3.4. *The shape of water bells*

The liquid film detaches from the impactor with the angle ψ_0 and we observe the resulting bell which can be open or closed, stable or unstable. We first concentrate on stable bells, the shapes of which remain stationary. The shapes of these stable bells have been qualitatively described in figure 7 and a new example is presented in figure 12(*a*), where the result of the edge detection algorithm is superposed on the picture as a black continuous line.

Applying this method to the different water bells presented in figure 7, we obtain the shape evolution presented in figure 12(*b*). This evolution shows that, even if the shape is not intrinsically altered by the velocity, the radial extent of the liquid sheet is very sensitive to that parameter: in figure 12(*b*), as the velocity is increased by the factor 3.4, from 1.08 to 3.67, the radial extent is multiplied by 10.6.

The first closed bell is the one corresponding to $U_0 = 2.65$ m s^{-1}. Above this limit, the bells are open as in figure 7(*m–o*) and one notices that the point where they break does not always correspond to the maximal diameter.

3.5. *The dynamics of formation of the bell*

The dynamics of formation of water bells is observed with a high-speed Kodak 4500HS video camera. Two examples of bell formation are presented in figures 13 and 14. In these figures, time increases from left to right and from top to bottom. Both sequences have been obtained using the same procedure: the water jet is initially established and we use a plastic hollow tube to deviate its trajectory from the impactor. When the setup of the camera is completed, the plastic tube is removed and we observe the impact of the jet on the disc. The main drawback of this procedure is that the leading edge of the jet is initially roughly defined as it can be seen in the first image of each sequence. However, this procedure ensures that the jet velocity and diameter
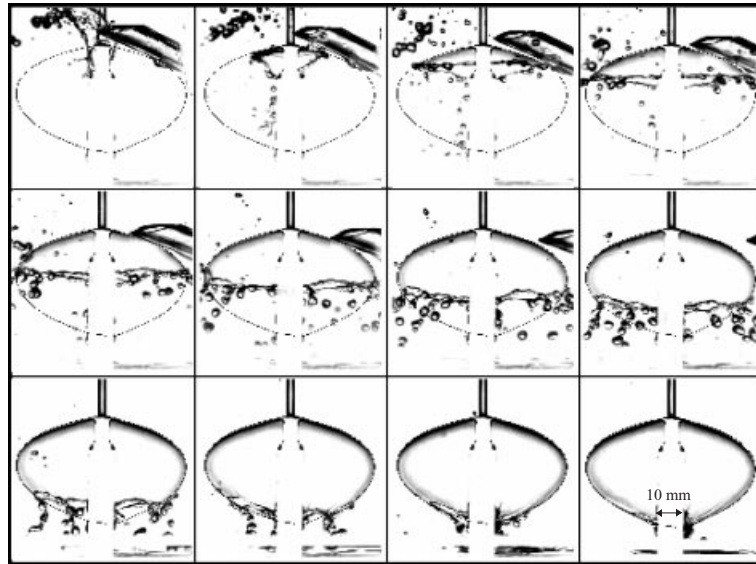
FIGURE 13. Dynamics of formation of the bell obtained with $D_0 = 3\,\mathrm{mm}$, $D_i = 7.33\,\mathrm{mm}$, $U_0 = 2.25\,\mathrm{m\,s^{-1}}$ and $\psi_0 = 74.7°$. Time increases from left to right and from top to bottom with the time step $\Delta t = 15.5\,\mathrm{ms}$.
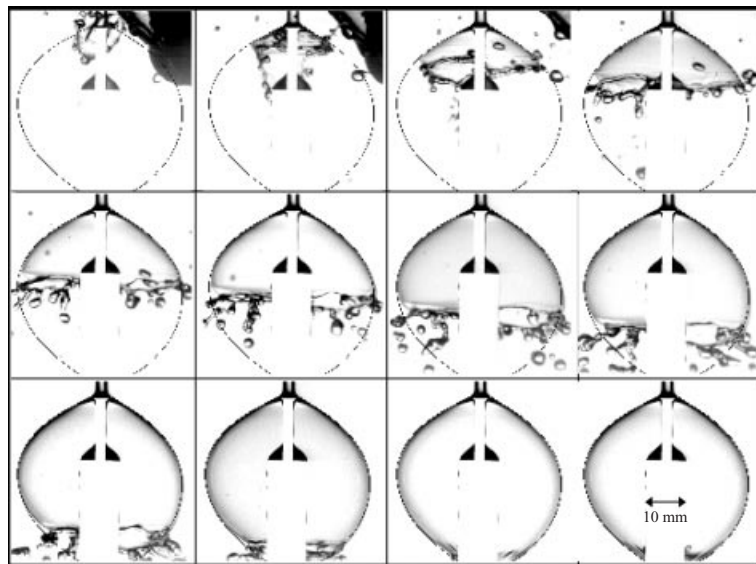

FIGURE 14. Dynamics of formation of the bell obtained with $D_0 = 3\,\mathrm{mm}$, $D_i = 4.0\,\mathrm{mm}$, $U_0 = 2.05\,\mathrm{m\,s^{-1}}$ and $\psi_0 = 61°$. Time increases from left to right and from top to bottom with the time step $\Delta t = 7.77\,\mathrm{ms}$.

remain constant over the whole formation process and allows a reasonable definition of the edge of the liquid sheet outside the impactor. The dotted line in each picture represents the stationary shape of the bell. This shape is extracted from an image captured one or two minutes after the end of the formation process. The first sequence presented in figure 13 corresponds to a 3 mm jet diameter impacting on a 7.33 mm disc with the velocity $U_0 = 2.25\,\mathrm{m\,s^{-1}}$. The corresponding ejection angle is $\psi_0 = 74.7°$ and the formation time T_f, is of the order of $11\Delta t \approx 170\,\mathrm{ms}$, where $\Delta t = 15.5\,\mathrm{ms}$ is the
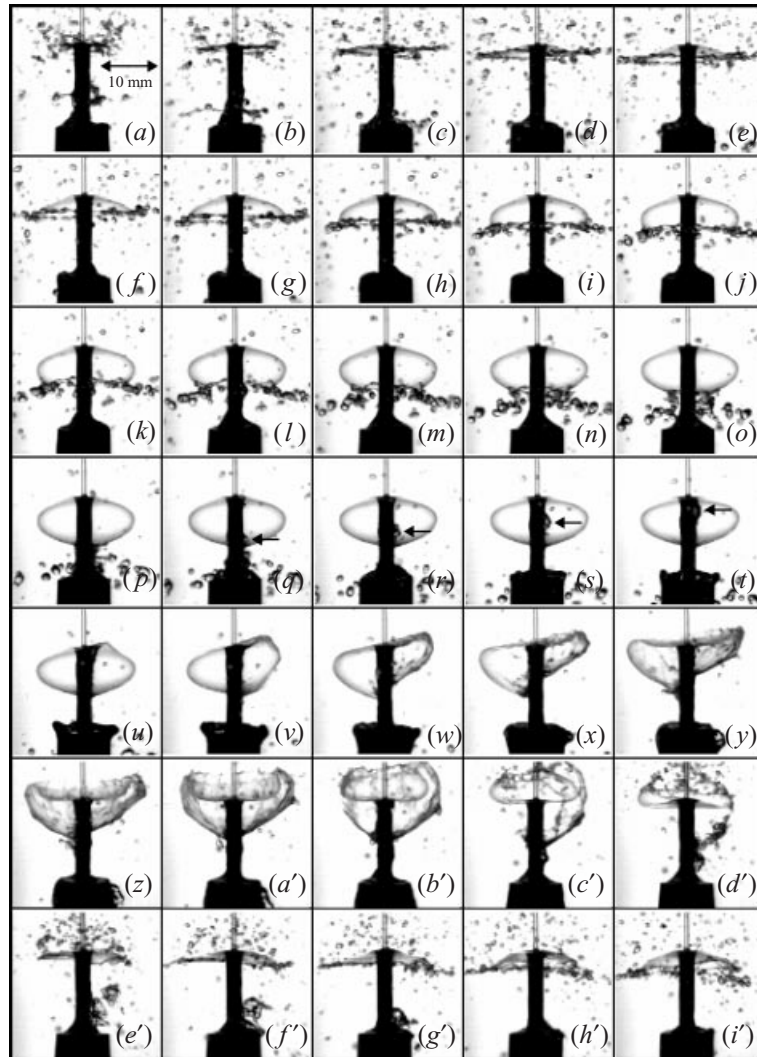
FIGURE 15. Instability of a closed water bell triggered by an upward moving liquid bulge, observed with $D_0 = 0.8$ mm, $D_i = 4.0$ mm, $U_0 = 5.33$ m s^{-1} and $\psi_0 = 75°$. Time increases from left to right and from top to bottom with the time step $\Delta t = 2.22$ ms.

time step between images. The trajectory of the edge of the sheet is characterized by an expanding phase followed by a contracting one. According to figure 13, both phases have approximately the same duration, $T_f/2$. It is also remarkable that the unsteady trajectory of the edge superposes on the steady trajectory of the liquid particles, defined by the stationary bell shape. For the same jet diameter, figure 14 presents the dynamics of formation of the bell obtained with $D_i = 4.0$ mm and $U_0 = 2.05$ m s^{-1}. The corresponding ejection angle is $\psi_0 = 61°$. This sequence is similar to the one just presented except that the time step is reduced by a factor of 2.

3.6. *Stability of water bells*

The discussion on stability that we develop in this article completes and expands the ideas presented in Clanet (2000). Stable water bells are characterized by a stationary shape which can be either closed or open. In this subsection, we consider unstable
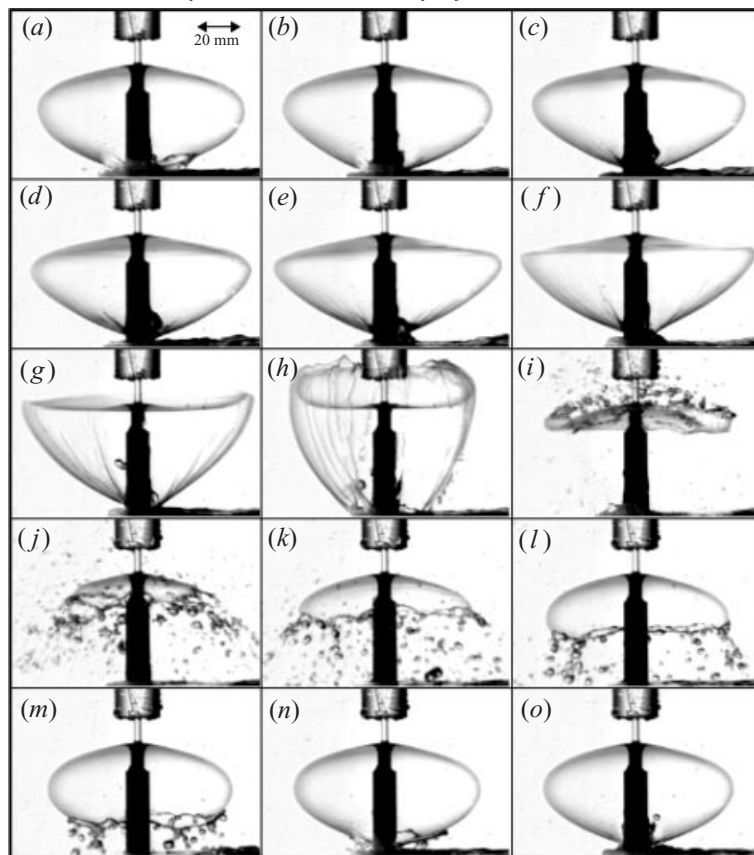
FIGURE 16. Instability of a closed water bell triggered by a pressure perturbation, observed with $\psi_0 = 77°$, $D_0 = 3.0$ mm, $D_i = 9.87$ mm and $U_0 = 2.7$ m s^{-1}. Time increases from (*a*) to (*o*) with the time step $\Delta t = 35.5$ ms.

bells, the shape of which changes with time, and we have already mentioned that these unstable bells are always closed.

Perhaps the more intuitive instability is the one presented in figure 15. In this figure, a 0.8 mm jet impacts on a 4 mm disc with the velocity $U_0 = 5.33$ m s^{-1} and forms a bell. As in the previous sequences, time increases from left to right and from top to bottom with the time step $\Delta t = 2.2$ ms. The dynamics of formation extends from (*a*) to (*p*) and is similar to the one presented in figures 13 and 14. However, following the closing of the bell, we observe that one part of the impinging liquid moves up towards the edges of the disc. This upward motion is indicated with arrows in figure 15(*q, r, s, t*). Once this bulge of liquid reaches the edge of the impactor, it destabilizes the whole liquid sheet, which undergoes a complete shape transformation prior to the formation of a new bell. The whole process is repeated periodically and in the case presented in figure 15 the period of creation–destruction, is of the order of $30\Delta t = 66$ ms. With this mechanism, the axisymmetry of the problem is broken when the bulge reaches the edge and the shape is tilted at the beginning of the transformation, indicating the point of impact of the bulge.

Another mechanism of instability is presented in figure 16. The time step is $\Delta t = 35.5$ ms and we observe a 3 mm jet impacting on a 9.87 mm disc with the velocity $U_0 = 2.7$ m s^{-1}. Starting the experiment with a stable open bell (*a*), we progressively decrease
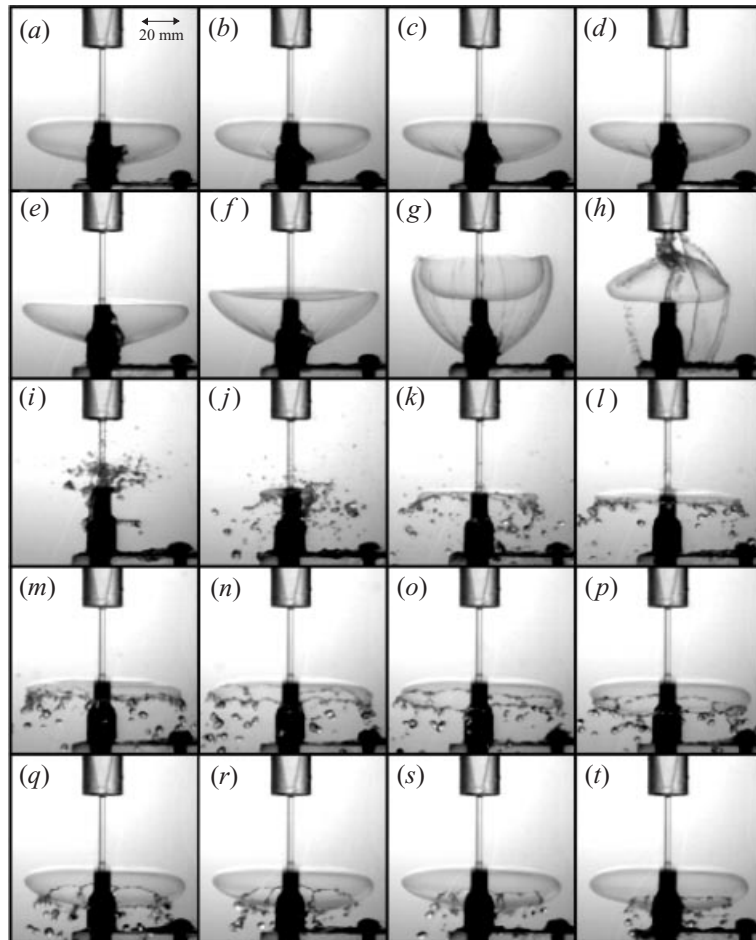
FIGURE 17. Instability of a closed water bell characterized by a large angle of ejection $\psi_0 = 87°$, observed with $D_0 = 3.0$ mm, $D_i = 10.0$ mm and $U_0 = 2.21$ m s^{-1}. Time increases from (*a*) to (*t*) with the time step $\Delta t = 27.7$ ms.

the flow rate. According to figure 12(*b*), this reduces the size of the bell, but as the bell closes the decrease of the flow rate starts to compress the air inside the bell. This pressure increase, at one point, destabilizes the whole bell with a similar scenario as the one observed in figure 15, except that here, the axisymmetry is conserved. This shape transformation leads to the bursting of the liquid sheet and thus to the equality of the pressure between the inside and the outside of the bell. The triggering mechanism is thus removed at the bursting and if we stop decreasing the flow rate when the bell closes, we obtain a stable bell, similar to the original one but a little smaller, since the flow rate has been reduced in between. If we continue to decrease the velocity, the bell will undergo a similar transformation and we can get up to 10 generations of bells, each smaller than the previous one and larger than the following one.

This cascade was noticed by Savart when he considered the emptying of a cylindrical tube through a thin hole of 12 mm perforated at the centre of the bottom part of the tube. Looking at the impact of the resulting vertical jet on a 27 mm disc, he reports:

for a liquid pressure of 32 to 33 cm of water column, the water bells close completely taking the shape of a solid of revolution with 40 cm in diameter and 45 cm in height,
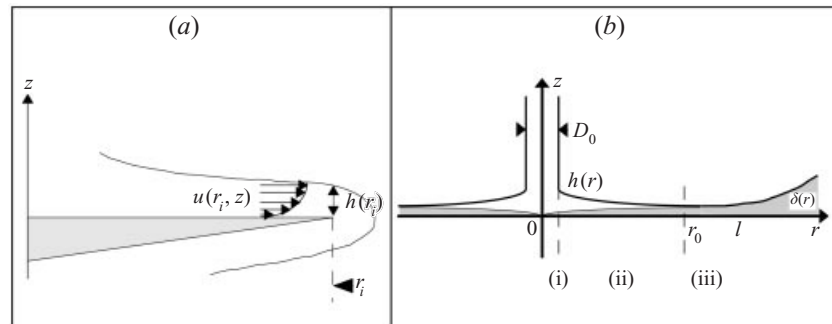
FIGURE 18. Presentation of the detachment problem: (*a*) structure of the flow at the edge of the disc, (*b*) structure of the flow in the film.

perfectly clear and with a curve generator that looks like a semi-lemniscate. From this time on, the bell decreases slowly in volume; but when the pressure does not exceed 10 to 12 cm, its shape changes rapidly and after a short time, the first shape is recovered. These instantaneous shape changes happen periodically up to 7 or 8 times until the bell always decreasing in volume completely disappears.

Perhaps the more puzzling instability is the one presented in figure 17, where a 3.0 mm jet impacts on a 10.0 mm impactor with the velocity $U_0 = 2.21\,\mathrm{m\,s^{-1}}$. In this experiment, the impactor is not flat but slightly conical so that the resulting liquid sheet is ejected with the angle $\psi_0 = 87°$. We observe that with a constant flow rate and without any bulge perturbation, the bell also undergoes an unstable cycle of creation and destruction with a period $T \approx 20\Delta t = 0.55\,\mathrm{s}$. During the whole transformation the axisymmetry is conserved and the resulting bell observed in (*t*) has the same dimensions as the initial one (*a*).

Although the origin of the three instabilities presented in figures 15, 16 and 17 is different, we observe that the response of the bell to recover its stability is almost the same in the three cases: the symmetry about the equatorial plane is first broken and the ejection angle increases up to a point where the bell changes its downward curvature for an upward one. This curvature switch leads to a closing of the liquid sheet onto the feeding jet which destroys the whole bell. In figures 15 and 16, we observe that the liquid film can also be broken during the curvature inversion and prior to the closing of the sheet on the jet.

4. Models

This section is devoted to the presentation and analysis of models intended to improve the understanding of the experimental results just described. The study of the flow is conducted using the nomenclature presented in figure 18(*b*), where *r* and *z* respectively are the radial and vertical axes, the origin of the coordinate system being the impact point of the jet. Also, $u(r, z)$ and $w(r, z)$ are the corresponding velocity components, and $h(r)$ the film thickness at the location *r*.

4.1. *On the detachment of the film from the impactor*

The problem of the detachment of the film at the edge of the impactor is presented in figure 18(*a*): the liquid film reaches the edge, $r_i \equiv D_i/2$, with the velocity profile $u(r_i, z)$, and the thickness $h(r_i)$. At this location, the inertia force $F_{in} \approx \rho \pi D_i \int_0^{h(r_i)} u(r_i, z)^2 \, \mathrm{d}z$ tends to detach the film whereas the capillary action $F_c \approx 2\sigma C S$ tries to keep the film

attached to the impactor. In this expression for the capillary force, $C \approx 1/h(r_i) + 1/r_i$ represents the total curvature of the liquid at the edge, and $S \approx \pi D_i h(r_i)$ the surface on which F_c is applied. The factor 2 accounts for the two sides of the liquid sheet when it detaches. The detachment of the film occurs when $F_{in} > F_c$. Using the above expressions for the forces, this criterion can be written

$$\int_0^{h(r_i)} u(r_i, z)^2 \, \mathrm{d}z > \frac{2\sigma}{\rho}\left(1 + \frac{h(r_i)}{r_i}\right). \tag{4.1}$$

The main factor we need to discuss the detachment problem is the remaining momentum flux in the film when it reaches the edge of the disc, $I(r_i) \equiv \int_0^{h(r_i)} u(r_i, z)^2 \, \mathrm{d}z$. The complete analysis of the radial spread of a liquid jet over a horizontal plane was performed by Watson (1964) and we just recall the origin of the results we need.

The inviscid limit of the spreading problem reduces to a potential flow with free streamlines, the solution of which can be written

$$u(r, z) = U_0, \quad w(r, z) = -U_0 z/r, \quad h(r) = \frac{1}{8}\frac{D_0^2}{r} = h_{min}. \tag{4.2}$$

This solution, valid for $r > D_0/2$, reveals a constant radial velocity and a film thickness decrease as $1/r$. This value of the film thickness is increased by the boundary layer and is therefore referred to as h_{min}, the minimum value of h. In this inviscid limit, the remaining momentum flux is simply

$$I(r) \equiv \int_0^{h(r)} u(r, z)^2 \, \mathrm{d}z = \frac{U_0^2 D_0^2}{8r} = I_{max}. \tag{4.3}$$

This value I_{max} is the maximum value of I since no losses have been considered. For the Reynolds number in the film, $Re_h \equiv U_0 h/v$, we get

$$Re_h(r) = \frac{1}{8}Re\frac{D_0}{r}. \tag{4.4}$$

As expected, the effect of viscosity increases with the radial distance r.

Considering the effect of viscosity, the boundary layer approximations reduce the description of the flow in the film to the set of equations

$$\frac{\partial u}{\partial r} + \frac{u}{r} + \frac{\partial w}{\partial z} = 0, \tag{4.5}$$

$$u\frac{\partial u}{\partial r} + w\frac{\partial u}{\partial z} = v\frac{\partial^2 u}{\partial z^2}, \tag{4.6}$$

where (4.5) ensures mass flux conservation and (4.6) describes the decrease of the film momentum due to viscosity. In the momentum evolution equation (4.6), the gravitational pressure term, $G \equiv g \, \mathrm{d}h/\mathrm{d}r$, has been neglected in front of the viscous term, $V \equiv v(\partial^2 u/\partial z^2)$. This assumption can be discussed using an order of magnitude analysis based on the inviscid results presented in (4.2), from which $G \simeq gD_0^2/(8r^2)$, and $V \simeq 64vU_0 r^2/D_0^4$, so that $V/G \simeq 512(r/D_0)^4 vU_0/(gD_0^2)$. Considering the range $r/D_0 > 1$, this ratio is always larger than 10 in our applications, which justifies the form of the momentum evolution equation (4.6). This system must be solved with the boundary conditions

$$u(r, 0) = w(r, 0) = 0, \tag{4.7}$$

$$\left.\frac{\partial u}{\partial z}\right|_{z=h(r)} = 0, \tag{4.8}$$

$$r\int_0^{h(r)} u(r,z)\,\mathrm{d}z = \tfrac{1}{8}D_0^2 U_0, \tag{4.9}$$

where the solid boundary conditions (4.7) are completed by a free surface condition with no shear (4.8) (the effect of the friction with the surrounding air is neglected) and by the constant-volume flux condition (4.9).

To integrate this system of boundary layer equations, we identify three different regions (respectively denoted (i), (ii) and (iii) in figure 18b):

(*a*) an internal region (i) defined by $r \sim D_0/2$ where the speed outside the boundary layer, δ, rises rapidly from 0 at the stagnation point to U_0, and the boundary layer thickness is $\delta \sim \sqrt{\nu D_0/U_0}$. In this region we will consider that $I \approx I_{max}$.

(*b*) an external region (ii and iii), defined by $r > D_0/2$, where the stream lines almost remain parallel and where we look for solutions of the type

$$u(r,z) = U(r)f(z/\delta(r)). \tag{4.10}$$

In this external region, we distinguish the region (ii) where the boundary layer $\delta(r)$, is smaller than the film thickness $h(r)$, and where the velocity outside the boundary layer is constant $U(r) = U_0$, from the region (iii), where the whole film thickness corresponds to the boundary layer, $h(r) = \delta(r)$, and where $U(r) < U_0$. The transition from (ii) to (iii) happens at the radial location r_0, defined by $h(r_0) = \delta(r_0)$.

In region (ii), the results obtained by Watson can by summarized as

$$\delta(r) \approx 2.586\sqrt{\frac{\nu r}{U_0}}, \tag{4.11}$$

$$h(r) \approx h_{min} + 0.385\delta(r), \tag{4.12}$$

and

$$I(r) \approx I_{max} - \frac{\delta(r)U_0^2}{7.16}. \tag{4.13}$$

Using equations (4.11) and (4.12), together with the definition of r_0, we can evaluate the location of the transition between regions (ii) and (iii) as

$$r_0 \approx 0.183 D_0 Re^{1/3}. \tag{4.14}$$

For a typical value $Re = 6000$, we observe that the transition occurs at 3.3 jet diameters.

In the self-similar region (iii), Watson shows that the flow in the film is characterized by the evolutions

$$h(r) = \delta(r) = D_0 \frac{4.83}{Re}\frac{r^3 + l^3}{D_0^2 r}, \tag{4.15}$$

$$U(r) \approx U_0 \frac{Re}{23.8}\frac{D_0^3}{r^3 + l^3}, \tag{4.16}$$

and

$$I(r) \approx \frac{Re}{246.5}\frac{D_0^4}{(r^3 + l^3)r}U_0^2 D_0. \tag{4.17}$$

The constant of integration, l, which appears in equations (4.15), (4.16) and (4.17) is determined by the condition that the free surface velocity $U(r)$ in (4.16) must be
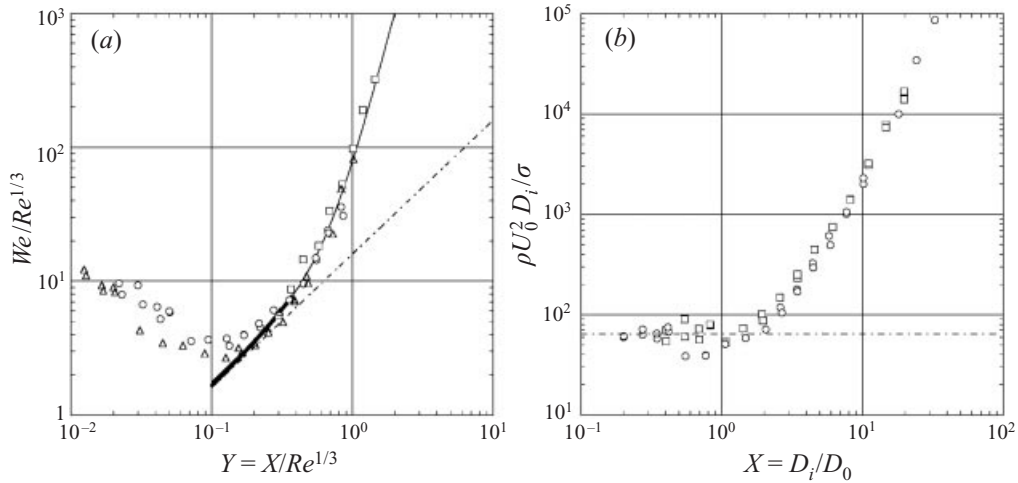
FIGURE 19. Detachment of the film from the impactor. (a) $X > 1$: □, $D_0 = 0.8$ mm; ○, $D_0 = 3.0$ mm; △, $D_0 = 6.0$ mm; dotted line, equation (4.21); bold continuous line, equation (4.19); thin continuous line, equation (4.20). (b) $X < 1$: □, $D_0 = 3.0$ mm; ○, $D_0 = 6.0$ mm; dotted line, $\rho U_0^2 D_i/\sigma = 62$.

equal to U_0 at $r = r_0$. This condition leads to

$$l \approx 0.329 D_0 Re^{1/3}. \tag{4.18}$$

We now have the full description of the radial spread of the jet over the disc in the different regions identified in figure 18(b) and we can concentrate on the detachment problem.

In the limit $X > 1$, where $h(r_i)/r_i \ll 1$, the criterion (4.1) reduces to $I(r_i) \geqslant K_1(2\sigma/\rho)$, where $K_1 > 1$ is a constant to be determined experimentally what indicates by what amount the momentum flux $I(r_i)$ has to be larger than the attaching capillary effect for the detachment to occur. Using the momentum flux expressions obtained in region (ii), this equality can be written

$$\frac{We}{Re^{1/3}} \geqslant 8K_1 \frac{Y}{1 - 1.02 Y^{3/2}}, \tag{4.19}$$

where $Y \equiv X/Re^{1/3}$. According to equation (4.14), this expression holds up to $Y = 0.366$. For larger values of Y, we use the expressions obtained in region (iii) which lead to

$$\frac{We}{Re^{1/3}} \geqslant 8.78 K_1 Y (1 + 3.51 Y^3). \tag{4.20}$$

The inviscid flow described by (4.3) can also be written in the form $We/Re^{1/3}(Y)$:

$$\frac{We}{Re^{1/3}} \geqslant 8K_1 Y. \tag{4.21}$$

Compared to the above two expressions (4.19) and (4.20), this inviscid limit (4.21) leads, for a given Y, to a smaller value of $We/Re^{1/3}$, meaning that viscosity also opposes the detachment. These results are compared to the experimental measurements in figure 19(a), where the experimental measurements presented in figure 10 are plotted in the plane $(We/Re^{1/3}, Y)$. For $Y > 0.2$, the results obtained with the different jet diameters collapse on a single curve. The constant K_1 is chosen so that the inviscid limit (4.21) is tangent to the experimental data. This procedure leads to $K_1 \approx 2.0$. Using this value, the relation (4.19) is presented as a bold line in the range $Y \in [0.1, 0.366]$ while equation (4.20) appears as a thin line in the range $Y > 0.1$. One
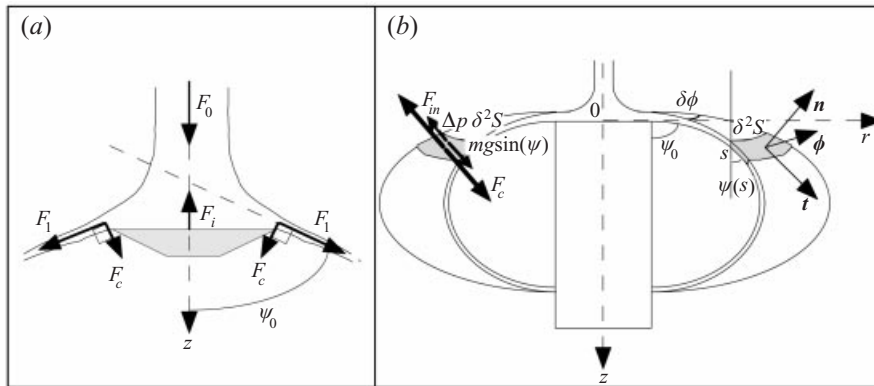
FIGURE 20. Equilibrium of a liquid sheet element: (*a*) at the edge of the impactor (*b*) far from the edge.

first notices that the behaviour of equation (4.20) is close to that of equation (4.19) in the range $Y \in [0.1, 0.366]$ where it is not supposed to apply. This is due to the matching procedure used to connect regions (ii) and (iii). Moreover, equation (4.20) is a good approximation of the behaviour observed experimentally for the whole range $Y > 0.2$.

In the limit $X < 1$, where $h(r_i)/r_i \gg 1$, equation (4.1) reduces to $I(r_i) \geqslant K_2 2\sigma h(r_i)/(\rho r_i)$, where K_2 is a constant to be determined experimentally, similarly to K_1. Using the description of the flow in region (1), $I(r_i) = I_{max}$, the above criterion takes the form

$$\frac{\rho U_0^2 D_i}{\sigma} \geqslant 4K_2. \tag{4.22}$$

This result is compared to the experimental measurements in figure 19(*b*), where the experimental measurements presented in figure 10 are plotted in the plane $(\rho U_0^2 D_i/\sigma, X)$. For $X < 1$, the experimental data are rather scattered but the constant behaviour predicted by equation (4.22) appears to be reasonable with $K_2 \approx 15.5$.

In summary, for given Reynolds and Weber numbers, the liquid film detaches if the diameter ratio X is in the range $X \in]X_-, X_+[$, where X_- is deduced from equation (4.22):

$$X_- = \frac{62}{We}, \tag{4.23}$$

and X_+ is implicitly given by equation (4.20):

$$17.6 \frac{X_+}{Re^{1/3}} \left[1 + 3.51 \left(\frac{X_+}{Re^{1/3}} \right)^3 \right] = \frac{We}{Re^{1/3}}. \tag{4.24}$$

4.2. On the angle of ejection

The model we propose to account for the evolution of the angle of ejection ψ_0 shown in figure 11, is presented in figure 20(*a*), where the bold arrows represent the different forces and momentum fluxes involved in the equilibrium of the liquid sheet at the edge of the impactor. F_i represents the force of the impactor, aligned with the axis of the jet, and F_c is the capillary force, normal to the sheet. Writing the vertical force balance, we obtain

$$\rho \pi D_i I(r_i) \cos(\psi_0) - \rho \pi D_i I_{max} = -F_i + F_c \sin(\psi_0). \tag{4.25}$$
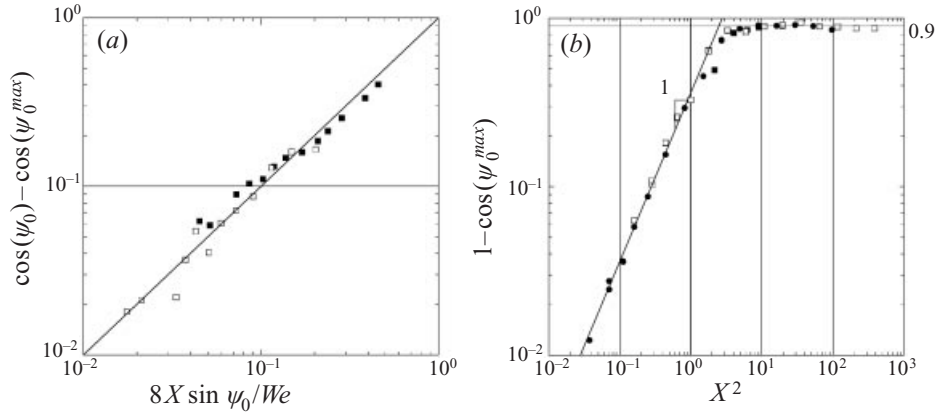
FIGURE 21. Evolution of the angle of ejection ψ_0: (a) with $8X \sin(\psi_0)/We$ (■, $D_0 = 3$ mm and $D_i = 9.87$ mm; □, $D_0 = 3$ mm and $D_i = 4$ mm); (b) with X^2, in the limit $We \gg 1$ (■, $D_0 = 0.8$ mm; □, $D_0 = 3.0$ mm; ●, $D_0 = 6.0$ mm).

Using the expression for the capillary force $F_c = 2C\sigma S$, with $C \approx 1/r_i + 1/h(r_i)$ and $S \approx 2\pi r_i h(r_i)$, equation (4.25) reduces to

$$\frac{I(r_i)}{I_{max}} \cos(\psi_0) - 1 = -\frac{4}{\pi} \frac{F_i}{\rho U_0^2 D_0^2} + \frac{8X}{We}\left(1 + \frac{h(r_i)}{r_i}\right)\sin(\psi_0). \qquad (4.26)$$

In the limit $We \gg 1$, the second term of the right-hand side of equation (4.26) can be neglected and the angle ψ_0^{max} only depends on the action of the impactor. Through the action–reaction law, F_i can be evaluated as $F_i = (C_1\pi/4)D_i^2\rho U_0^2$ in the limit $X < 1$ and as $F_i = (C_2\pi/4)D_0^2\rho U_0^2$ in the limit $X > 1$. The constants C_1 and C_2 are to be determined experimentally.

In the low-viscosity limit, $I(r_i)/I_{max} \approx 1$, and equation (4.26) reduces to

$$1 - \cos(\psi_0^{max}) = C_1 X^2 \quad \text{for } X < 1, \qquad (4.27)$$

and

$$1 - \cos(\psi_0^{max}) = C_2 \quad \text{for } X > 1. \qquad (4.28)$$

The function $[1 - \cos(\psi_0^{max})](X^2)$ is presented in figure 21(b). In the limit $X < 1$, the linear evolution of $[1 - \cos(\psi_0^{max})]$ with X^2 is observed and the constant C_1 can be evaluated as $C_1 \approx 0.352$. This behaviour holds up to $X = 1$. Above this value, $[1 - \cos(\psi_0^{max})]$ remains almost constant as described by equation (4.28) with $C_2 \approx 0.9$. For moderate Weber numbers, the influence of F_c cannot be neglected and equation (4.26) can be written, using the results for ψ_0^{max},

$$\cos(\psi_0) - \cos(\psi_0^{max}) = \frac{8X}{We} \sin(\psi_0). \qquad (4.29)$$

This equation for ψ_0 is valid in the limit $h(r_i)/r_i \ll 1$. The function $[\cos(\psi_0) - \cos(\psi_0^{max})]$ is plotted versus $(8X \sin(\psi_0)/We)$ in figure 21(a) for the two cases presented in figure 11(a). The linear relationship described by equation (4.29) is observed with a one-to-one correspondence.

4.3. *On the shape of the bells*

Let us now consider the problem of the shape of water bells, using the notation presented in figure 20(*b*). Notice that the *z*-axis is now pointing downwards, in the flow direction.

The mass flux conservation at the curved location *s* takes the form

$$reu = \tfrac{1}{8}D_0^2 U_0, \tag{4.30}$$

where *r*, *e* and *u* respectively stand for the radial location, the film thickness and the local velocity at the distance *s* from the detaching point. The momentum evolution of the shaded element of surface $\delta^2 S$, presented in figure 20(*b*) is first considered along the tangent vector *t*, and leads to the evolution of the velocity

$$u^2 = u_e^2 + 2gz, \tag{4.31}$$

where $u_e \equiv \sqrt{I(r_i)/h(r_i)}$ is the equivalent momentum velocity at the edge of the impactor. Its value can be determined with the values of $I(r_i)$ and $h(r_i)$ obtained in the three different zones identified in §4.1.

In the direction $-\boldsymbol{n}$, normal to the propagation, the equilibrium of the element is achieved through the balance of capillary forces $F_c = 2C\sigma\delta^2 S$, and gravity $mg\sin(\psi)$, with the centrifugal force mu^2/R_c, and the pressure difference action $p\delta^2 S$:

$$(2C\sigma - p)\delta^2 S + mg\sin(\psi) = m\frac{u^2}{R_c}, \tag{4.32}$$

where $m \equiv \rho\delta^2 Se$, is the mass of the element and $C \equiv 1/R_c + \cos(\psi)/r$, its total curvature, the sum of the two principle curvatures, $1/R_c$, in the $(\boldsymbol{n}, \boldsymbol{t})$ plane and $\cos(\psi)/r$, in the $(\boldsymbol{n}, \boldsymbol{\phi})$ plane. In equation (4.32), *p* is the pressure difference between the inside and the outside of the bell. This difference is zero when the bell is open but can be different from zero in the case of closed bells. Using U_0 and $L = D_0 We/16$, as the characteristic speed and length, the above equations (4.31) and (4.32) are respectively reduced to

$$\tilde{u}^2 = \tilde{u}_e^2 + 2\beta\tilde{z}, \tag{4.33}$$

and

$$(\tilde{u} - \tilde{r})\frac{d\psi}{d\tilde{s}} = -\cos(\psi) + \alpha\tilde{r} - \beta\frac{\sin(\psi)}{\tilde{u}}, \tag{4.34}$$

where $\alpha \equiv pL/(2\sigma)$ is the reduced pressure difference and $\beta \equiv gL/U_0^2$ the reduced gravity. All the dimensionless quantities are indicated with a tilde except angles. This system of equations (4.33) and (4.34) has to be integrated with the initial conditions $\tilde{r}(0) = \tilde{r}_i$ and $(d\tilde{r}/d\tilde{z})_{\tilde{z}=0} = \tan(\psi_0)$.

The reduced momentum velocity $\tilde{u}_e \equiv \sqrt{I(r_i)/(h(r_i)U_0^2)}$, traces the viscous losses on the impactor. In the inviscid limit described by equations (4.2) and (4.3), we find $\tilde{u}_e = 1$. In the region (ii), equations (4.12) and (4.13) lead to

$$\tilde{u}_e \approx \sqrt{\frac{1 - 1.02(X/Re^{1/3})^{3/2}}{1 + 2.816(X/Re^{1/3})^{3/2}}}. \tag{4.35}$$

In the limit $X/Re^{1/3} \ll 1$, we recover $\tilde{u}_e \approx 1$ and at the end of region (2), where $X/Re^{1/3} = 0.366$ (see equation (4.14)), we find $\tilde{u}_e \approx 0.7$. Finally, in the self-similar

region (3), equations (4.15) and (4.17) lead to

$$\tilde{u}_e \approx 0.812 \frac{1}{1 + 3.5(X/Re^{1/3})^3}. \tag{4.36}$$

At the matching point r_0, $X/Re^{1/3} = 0.366$, we recover $\tilde{u}_e \approx 0.7$ and in the limit $X/Re^{1/3} \gg 1$ we find $\tilde{u}_e \approx 0.286 Re/X^3$.

In the limit $\alpha = 0$ and $\beta \gg 1$, where the effect of gravity overcomes surface tension, the system (4.33) and (4.34) reduces to

$$-\tilde{u}^2 \frac{d\psi}{d\tilde{s}} = \beta \sin(\psi), \tag{4.37}$$

the solution of which is the paraboloid

$$\tilde{z} = \frac{\beta}{2\tilde{u}_e^2}(\tilde{r} - \tilde{r}_i)^2. \tag{4.38}$$

In that limit, the fluid particles at the edge of the disc are independent and fall under their own weight.

In the limit $\alpha = 0$ and $\beta \ll 1$, surface tension effects dominate and the system (4.33) and (4.34) reduces to

$$\tilde{u} = \tilde{u}_e, \tag{4.39}$$

and

$$(\tilde{u} - \tilde{r}) \frac{d\psi}{d\tilde{s}} = -\cos(\psi). \tag{4.40}$$

The integration of the system (4.39) and (4.40) leads to the catenary

$$\tilde{r} = \tilde{u}_e - c_1 \cosh\left(\frac{\tilde{z} - c_2}{c_1}\right), \tag{4.41}$$

with the constants of integration

$$c_1 = (\tilde{u}_e - \tilde{r}_i)\cos(\psi_0) \quad \text{and} \quad c_2 = c_1 \ln\left(\frac{1 + \sin(\psi_0)}{\cos(\psi_0)}\right). \tag{4.42}$$

The catenary solution was first published in a slightly different form, in 1869, 36 years after Savart's work, by a 27 year old self-educated man, Joseph Boussinesq. The non-dimensional version of the solution was later produced by Taylor (1959). Compared to the paraboloid, this latter shape exhibits a symmetry with respect to the equatorial plane defined by $d\tilde{r}/d\tilde{z} = 0$. This symmetry is broken as soon as gravity starts to play a role.† This break in symmetry is further discussed in §4.6.

The gravitational domain that leads to the paraboloid and the capillary domain that leads to the catenary are separated by a critical value of β, that corresponds by definition to $\beta \equiv gL/U_0^2 = (D_0/a)^2/8$, where $a \equiv \sqrt{2\sigma/(\rho g)}$ is the capillary length of the liquid–air interface (for water on Earth, $a \approx 3.8\,\text{mm}$). To consider the effect of D_0 presented in figure 8, we evaluate $\beta \approx 0.31$ for figure 8(a) and $\beta \approx 0.078$ for 8(b). Since the asymmetry introduced by the effect of gravity is clearly observed in figure 8(a), we deduce that the symmetrical bell domain is determined by the threshold value $\beta \leqslant 0.1$, or $Bo \equiv D_0/a \leqslant 1$.

For $\beta = 0.07$, the exact solution for the bell shape given by (4.41) and (4.42), is compared to measured profiles in figure 22 for a large range of Weber numbers

---

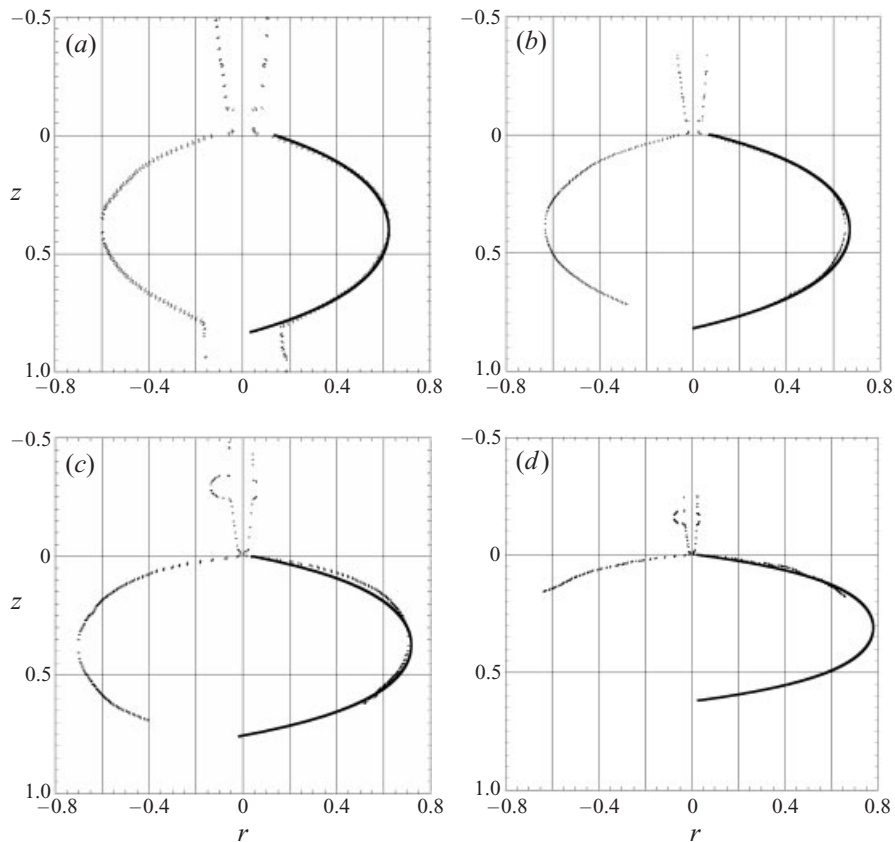† Looking at horizontal bells, G. I. Taylor (1959) has shown that air entrainment can also break the symmetry of the bells.

FIGURE 22. Comparison between the measured bell shape and the theoretical catenary: (a) $u_e = 0.84$, $r_i = 0.139$, $\psi_0 = 72°$; (b) $u_e = 0.86$, $r_i = 0.071$, $\psi_0 = 76°$; (c) $u_e = 0.88$, $r_i = 0.040$, $\psi_0 = 79°$; (d) $u_e = 0.89$, $r_i = 0.022$, $\psi_0 = 82.5°$.

$220 \leqslant We \leqslant 1350$. The experiments reported in figure 22 were conducted with $\alpha = 0$, using a straw to connect the inside of the bell to the outside. In all the cases, the catenary is a good approximation of the actual profile.

4.4. *On the dynamics of formation of water bells*

The problem of the formation of the bells is to determine the trajectory $s_f(t)$ of the liquid sheet front, just after the impact of the jet on the disc. As the bell is open during its formation, no pressure effect has to be considered, $\alpha = 0$, and we conduct the following discussion in the low-gravity limit $\beta < 0.1$, so that the stationary water bell expected at the end of the formation process is the Boussinesq catenary described by equations (4.41) and (4.42). The formation problem is presented in figure 23, where $s(t) = u_e t$ is the curvilinear position that the front would have if the bell was fully formed and $s_f(t)$ the actual front position. The front is characterized by its mass $M_f(t)$ and its velocity $u_f(t)$. The time evolution of $M_f(t)$ is due to the incoming fluid at the velocity u_e:

$$\frac{\mathrm{d}M_f}{\mathrm{d}t} = \rho \frac{\pi D_0^2}{4} \frac{U_0}{u_e} (u_e - u_f). \tag{4.43}$$
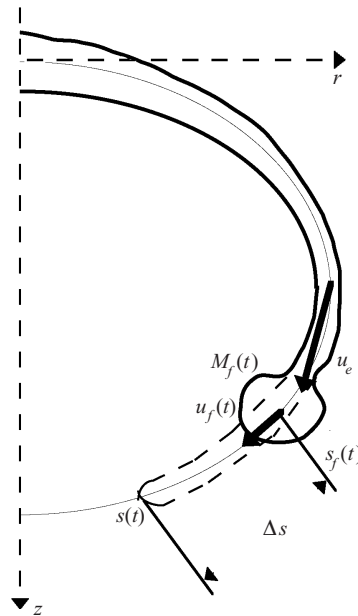
FIGURE 23. Presentation of the formation problem.

In the limit $u_f = u_e$, the front is not fed and its mass remains constant. In the limit where $u_f = 0$, the time evolution of the mass is equal to the mass flow rate of the jet $Q \equiv \rho\pi D_0^2 U_0/4$. The evolution of the momentum of the front $M_f u_f$ is due to the pushing action of the feeding liquid and to the retracting capillary force $f_c = 4\pi r_f \sigma$, where r_f is the radial location of the front. This force is aligned with the tangent vector $-\boldsymbol{t}$ and does not alter the equilibrium in the $\boldsymbol{n}$-direction. This explains the behaviour observed experimentally in figures 13 and 14, according to which the front trajectory corresponds to the stationary bell shape. The evolution of the momentum of the front takes the form

$$\frac{\mathrm{d}(M_f u_f)}{\mathrm{d}t} = -4\pi r_f \sigma + \frac{\mathrm{d}M_f}{\mathrm{d}t} u_e. \tag{4.44}$$

The system of equations (4.43) and (4.44) has to be solved with the initial conditions $u_f(0) = u_e$ and $M_f(0) = 0$. Using the variables $\Delta u \equiv u_e - u_f$ and $\mathrm{d}\Delta s/\mathrm{d}t \equiv \Delta u$, the system reduces to

$$\frac{\mathrm{d}M_f}{\mathrm{d}\Delta s} = \frac{Q}{u_e}, \tag{4.45}$$

and

$$\frac{\mathrm{d}^2(\Delta s)^2}{\mathrm{d}t^2} = \frac{4\sigma}{\rho e}, \tag{4.46}$$

with the initial conditions $\Delta s(0) = 0$ and $\Delta u(0) = 0$. Using the assumption that the film thickness e changes slowly, the system can be integrated with the solutions $M_f = Q/u_e \Delta s$ and $\Delta u = \sqrt{2\sigma/(\rho e)}$. With this quasi-steady assumption, the dynamics of the front is governed by the equation

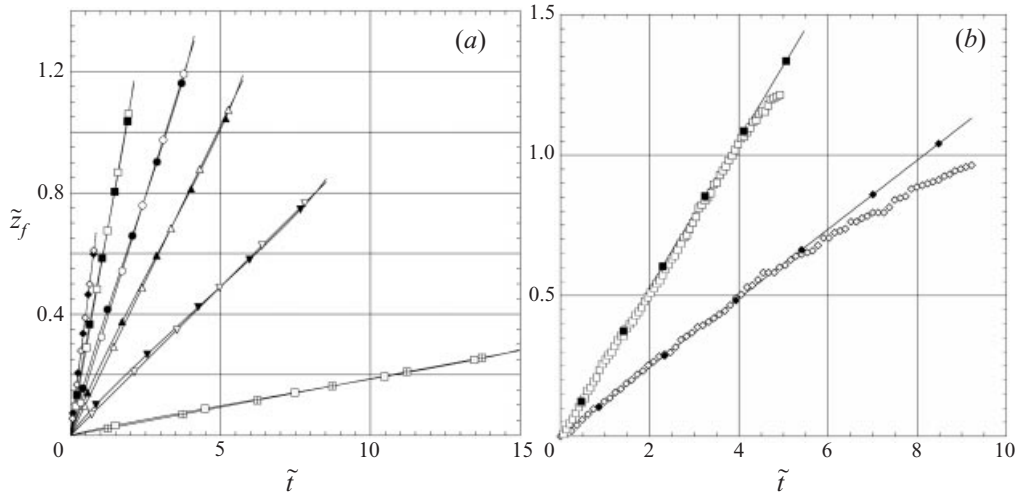$$\frac{\mathrm{d}s_f}{\mathrm{d}t} = u_e - \sqrt{\frac{2\sigma}{\rho e(r)}}, \tag{4.47}$$

FIGURE 24. Study of the trajectory $\tilde{z}_f(t)$. (*a*) Comparison of the numerical integration of equation (4.49) (NI) with the approximation (4.51) (AP): ◆, $\psi_0 = 20°$ NI; ◇, $\psi_0 = 20°$ AP; ■, $\psi_0 = 40°$ NI; □, $\psi_0 = 40°$ AP; ●, $\psi_0 = 60°$ NI; ○, $\psi_0 = 60°$ AP; ▲, $\psi_0 = 70°$ NI; △, $\psi_0 = 70°$ AP; ▼, $\psi_0 = 80°$ NI; ▽, $\psi_0 = 80°$ AP; ⊡, $\psi_0 = 88°$ NI; ⊞, $\psi_0 = 88°$ AP. (*b*) Comparison between the linear approximation (4.51) and the experimental measurements: ◇, experimental data $\psi_0 = 74.7°$, $\tilde{u}_e = 0.9$, $\tilde{r}_i = 0.09$; ◆, linear approximation in the same conditions; □, experimental data $\psi_0 = 60.2°$, $\tilde{u}_e = 0.92$, $\tilde{r}_i = 0.06$; ■, linear approximation in the same conditions.

where $e(r) = D_0^2 U_0/(8ru_e)$. Using U_0 and $L = D_0 We/16$ for the non-dimensionalization, we obtain

$$\frac{\mathrm{d}\tilde{s}_f}{\mathrm{d}\tilde{t}} = \tilde{u}_e - \sqrt{\tilde{r}_f}\sqrt{\tilde{u}_e}, \tag{4.48}$$

where $\tilde{r}_f$ is given by equation (4.41). The characteristic time is obviously L/U_0. Since $\mathrm{d}\tilde{s}_f = \mathrm{d}\tilde{z}_f\sqrt{1 + (\mathrm{d}\tilde{r}_f/\mathrm{d}\tilde{z}_f)^2}$, equation (4.48) can be written

$$\frac{\mathrm{d}\tilde{z}_f}{\mathrm{d}\tilde{t}} = \tilde{u}_e \frac{1 - \sqrt{1 - (c_1/\tilde{u}_e)\cosh((\tilde{z} - c_2)/c_1)}}{\cosh((\tilde{z} - c_2)/c_1)}. \tag{4.49}$$

This ODE has to be integrated with the initial condition $\tilde{z}_f(0) = 0$. Its right-hand side remains almost constant from $\tilde{z}_f = 0$ to the maximal location $\tilde{z}_f = 2c_2$, where the bell closes on the axis. To evaluate this constant, we use the average value of the hyperbolic cosine:

$$\overline{\cosh\left(\frac{\tilde{z} - c_2}{c_1}\right)} \equiv \frac{1}{2c_2}\int_0^{2c_2}\cosh\left(\frac{\tilde{z} - c_2}{c_1}\right)\mathrm{d}z = \frac{c_1}{c_2}\tan(\psi_0). \tag{4.50}$$

With this mean value, we approximate equation (4.49) as

$$\tilde{z}_f = \tilde{V}_f\tilde{t} \quad \text{where} \quad \tilde{V}_f = \tilde{u}_e\frac{1 - \sqrt{1 - (c_1/\tilde{u}_e)(c_1/c_2)\tan(\psi_0)}}{(c_1/c_2)\tan(\psi_0)}. \tag{4.51}$$

This approximation is compared to the numerical integration of equation (4.49) in figure 24(*a*). Keeping $\tilde{u}_e = 1$ and $\tilde{r}_i = 0$, ψ_0 was increased from $20°$ to $88°$. In all the cases, the linear approximation (4.51) remains close to the numerical integration of the ODE (4.49).

The model we propose for the dynamics predicts a quasi-constant vertical velocity of the leading edge of the liquid sheet during the formation of the bell. This result
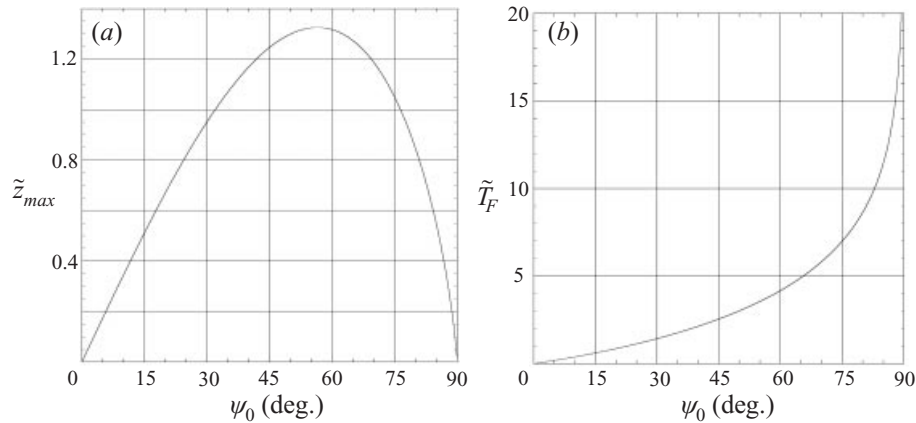
FIGURE 25. Characteristics of water bells: (*a*) evolution of longitudinal extension $\tilde{z}_{max}$ with the angle of ejection ψ_0; (*b*) evolution of the formation time $\tilde{T}_F$ with the angle of ejection ψ_0.

is compared in figure 24(*b*) to the experimental data presented in figures 13 and 14. In both cases, the linear approximation is within a few percent of the experimental trajectories.

To consider the location where the bell closes $\tilde{z}_{max} \equiv 2c_2$, we present in figure 25(*a*), the evolution of $\tilde{z}_{max}(\psi_0)$ obtained using the definition of c_2 in equation (4.42). This evolution reveals the existence of a maximum value $\tilde{z}_{max} \approx 1.32$ obtained with $\psi_0 \approx 56.5°$.

Using $\tilde{z}_{max}$, we can evaluate the formation time $\tilde{T}_F \approx \tilde{z}_{max}/\tilde{V}_f$. In the limit $\tilde{r}_i \ll 1$, this formation time becomes a function of ψ_0 only:

$$\tilde{T}_F \approx \frac{2\sin(\psi_0)}{1 - \sqrt{1 - \dfrac{\sin(\psi_0)}{\ln[(1+\sin\psi_0)/\cos\psi_0]}}}. \tag{4.52}$$

This function is presented in figure 25(*b*) where we observe a nonlinear increase of the $\tilde{T}_F$ with the angle of ejection.

4.5. *On the stability of water bells*

Three different examples of instability of bells have been presented in figures 15, 16 and 17. The first remark on stability concerns the influence of the pressure difference, p, between the inside and the outside of the bell. If that difference is kept equal to zero, for example using a straw that connects both sides, the resulting bells always remain stable. The origin of the bells' stability thus lies in the pressure difference effect, or more precisely in the reaction of the bell to a pressure difference perturbation. Let us first imagine that following a pressure increase inside the bell, the volume of the whole bell increases. In that case, the reaction of the bell tends to compensate the origin of the perturbation and one expects the bell to remain stable. On the other hand, if the bell volume decreases following a pressure increase, the bell reaction amplifies the perturbation and one may expect, in the end, the full bursting of the bell. This analysis leads to the stability criterion

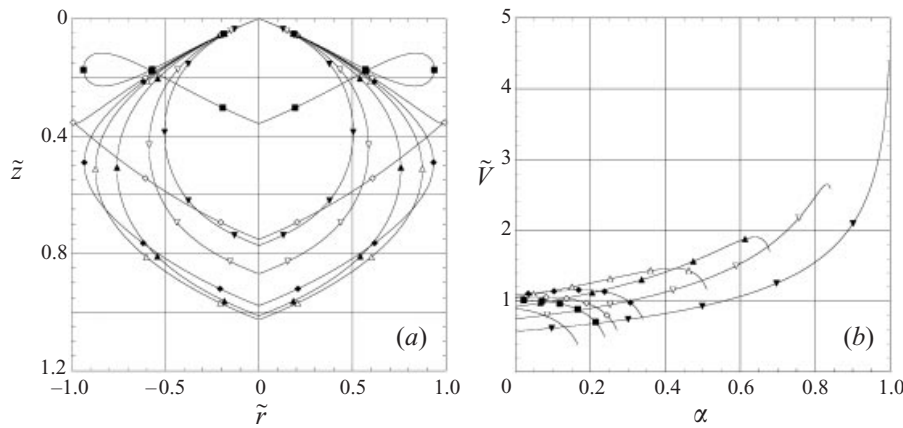$$\frac{\mathrm{d}V}{\mathrm{d}p} \geqslant 0, \tag{4.53}$$

FIGURE 26. Influence of the reduced pressure difference α. (a) Evolution of the shape of water bells with α for $\psi_0 = 76°$, $\tilde{u}_e = 1$: $-\blacktriangledown-$, $\alpha = -2$; $-\triangledown-$, $\alpha = -1$; $-\blacktriangle-$, $\alpha = 0$; $-\triangle-$, $\alpha = 0.3$; $-\blacklozenge-$, $\alpha = 0.4$; $-\lozenge-$, $\alpha = 0.5$; $-\blacksquare-$, $\alpha = 0.7$. (b) Evolution of the water bells volume with α, $\tilde{u}_e = 1$, $\tilde{r}_i = 0$: $-\blacktriangledown-$, $\psi_0 = 60°$; $-\triangledown-$, $\psi_0 = 65°$; $-\blacktriangle-$, $\psi_0 = 70°$; $-\triangle-$, $\psi_0 = 75°$; $-\blacklozenge-$, $\psi_0 = 80°$; $-\lozenge-$, $\psi_0 = 82°$; $-\blacksquare-$, $\psi_0 = 83°$; $-\square-$, $\psi_0 = 85°$.

where V is the volume of the closed bell. Looking at the system (4.33) and (4.34) in the limit $\beta \ll 1$, we find that $V \equiv L^3 \pi \int_0^{\tilde{z}_{max}} \tilde{r}^2 \, \mathrm{d}\tilde{z}$ is a function of three parameters $V(L, \alpha, \psi_0)$. Noticing that L and p are independent, the stability criterion (4.53) can be written

$$\frac{\mathrm{d}\tilde{V}}{\mathrm{d}p} = \frac{1}{L^3}\frac{\mathrm{d}V}{\mathrm{d}p} = \left(\frac{\partial\tilde{V}}{\partial\alpha}\right)_{\psi_0}\frac{L}{2\sigma} + \left(\frac{\partial\tilde{V}}{\partial\psi_0}\right)_\alpha\frac{\mathrm{d}\psi_0}{\mathrm{d}p}. \tag{4.54}$$

We first concentrate on the case where the first term on the right-hand side of equation (4.54) dominates, that is where ψ_0 remains almost constant and where the driving mechanism is the reduced pressure difference α. This effect is discussed on the basis of the following equation:

$$(\tilde{u}_e - \tilde{r})\frac{\mathrm{d}\psi}{\mathrm{d}\tilde{s}} = -\cos(\psi) + \alpha\tilde{r}, \tag{4.55}$$

that is deduced from equation (4.34), using the assumption that gravity is negligible. The effect of the pressure difference α on the shape of water bells is presented in figure 26(a), for $\alpha \in [-2, 0.7]$ and with the arbitrary angle $\psi_0 = 76°$. The initial conditions used for the numerical integration are $\psi = \psi_0$ at $\tilde{r} = 0$ and $\tilde{u}_e = 1$. The evolution of the shape with increasing values of the parameter α reveals that water bells tend to form a loop for a particular value of α_c ($\alpha_c \simeq 0.5$ in figure 26a). This loop formation is reminiscent of the shape of the bells during destabilization. However, note that the destabilization is strongly time dependent whereas the shapes presented in figure 26(a) are deduced from the stationary equation (4.55). The loop formation observed in figure 26(a), just signals the breakdown of the model. To approach the disintegration scenario, more analytical work on the time-dependent solution has to be done.

Projecting equation (4.55) on the $\tilde{r}$- and $\tilde{z}$-axes, leads to the system

$$\frac{\mathrm{d}}{\mathrm{d}\tilde{s}}\left[(\tilde{u}_e - \tilde{r})\frac{\mathrm{d}\tilde{r}}{\mathrm{d}\tilde{s}} + \tilde{s}\right] = \alpha\tilde{r}\frac{\mathrm{d}\tilde{z}}{\mathrm{d}\tilde{s}}, \tag{4.56}$$

$$(\tilde{u}_e - \tilde{r})\frac{\mathrm{d}\tilde{z}}{\mathrm{d}\tilde{s}} + \frac{\alpha}{2}\tilde{r}^2 = \cos(\psi_0). \tag{4.57}$$

FIGURE 27. Stable cusp observed for $\psi_0 = 52°$.

The second equation is derived in the limit $\tilde{r}_i = 0$. Applied at the location $\tilde{r}_1$ satisfying $(\mathrm{d}\tilde{z}/\mathrm{d}\tilde{s})_{\tilde{r}_1} = 0$, equation (4.57) gives $\alpha\tilde{r}_1^2 = 2\cos(\psi_0)$. In the same way, at the location $\tilde{r}_2$ defined by $(\mathrm{d}\tilde{r}/\mathrm{d}\tilde{s})_{\tilde{r}_2} = 0$, equation (4.57) gives $(\tilde{u}_e - \tilde{r}_2) + \alpha\tilde{r}_2^2/2 = \cos(\psi_0)$. At the first loop location, $\tilde{r}_1 = \tilde{r}_2 = \tilde{r}_c$ and one deduces from the above relations that

$$\tilde{r}_c = \tilde{u}_e \quad \text{and} \quad \alpha_c = \frac{2\cos(\psi_0)}{\tilde{u}_e^2}. \tag{4.58}$$

With $\psi_0 = 76°$, we find $\alpha_c = 0.48$.

In the limit where the first term of equation (4.54) dominates, the stability problem is reduced to the study of the sign of $(\partial\tilde{V}/\partial\alpha)_{\psi_0}$. The function $\tilde{V}(\alpha)$ is presented in figure 26(b) for different values of ψ_0 and in the range $\alpha \in [0, \alpha_c[$.

In the domain $\psi_0 \leqslant 60°$, the stability criterion is always satisfied. In this range, one could expect cusped shapes to be stable. This is actually the case, as shown in figure 27 where we present a stationary cusped bell obtained for $\psi_0 = 52°$. In the range $\psi_0 \geqslant 83°$, the stability criterion is never satisfied and the bells are unstable for all values of α. For $\psi_0 \in [60°, 83°]$ there is a value $\alpha^\star$, smaller than α_c, above which the bell becomes unstable. This unstable domain is presented shaded in figure 28(a). One notices in this figure that if $\psi_0 \in [60°, 83°]$, then $\alpha = 0$ corresponds to a stable bell. Since the instability leads to the bursting of the bell and thus to $\alpha = 0$ one expects the instability driven by the pressure increase α to occur once. This limit corresponds to the instability presented in figure 16.

If the pressure increase procedure is repeated, then a new instability is observed and as we have already mentioned in § 3.6 up to ten generations of bells can be observed. The function $D_{j+1}(D_j)$, where D_j and D_{j+1} respectively represent the maximal diameter of the mother and the daughter, is presented in figure 28(b) for the two different diameters $D_0 = 0.8\,\text{mm}$ and $D_0 = 3.0\,\text{mm}$. This figure reveals that $D_{j+1} \approx 0.82 D_j$.

This linear relationship is discussed by considering the bell as a membrane insulating the inside from the outside and characterized by a mean thickness $\bar{e}$ and the two spatial average curvatures $\overline{C_1}$ and $\overline{C_2}$, defined as

$$\overline{C_1} = \frac{\tilde{F}}{L} \quad \text{with} \quad \tilde{F} = \frac{1}{\tilde{z}_{max}} \int_0^{\tilde{z}_{max}} \frac{\mathrm{d}\psi}{\mathrm{d}\tilde{s}}\,\mathrm{d}\tilde{z}, \tag{4.59}$$
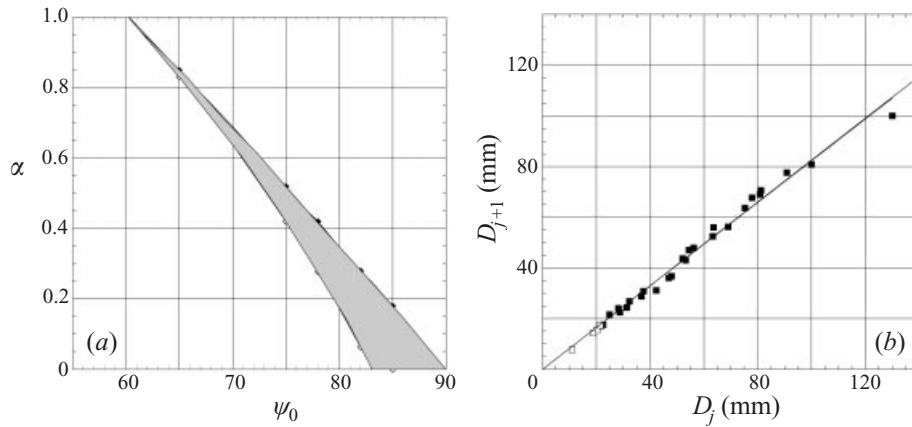
FIGURE 28. (a) Evolution of the unstable region $\alpha \in [\alpha^\star, \alpha_c]$ with the ejection angle ψ_0. (b) Relation between the daughter size D_{j+1} and the mother size D_j: $\square$, $D_0 = 0.8\,\text{mm}$; $\blacksquare$, $D_0 = 3.0\,\text{mm}$.

and

$$\overline{C_2} = \frac{\tilde{G}}{L} \quad \text{with} \quad \tilde{G} = \frac{1}{\tilde{z}_{max}} \int_0^{\tilde{z}_{max}} \frac{\cos(\psi)}{\tilde{r}} \, d\tilde{z}, \tag{4.60}$$

where $L = D_0 We/16$ is the characteristic length in the problem. In the case where the inside and the outside have the same pressure, the membrane equilibrium results from a competition between inertia and curvature: $2\sigma(\overline{C_1} + \overline{C_2}) = \rho \bar{e} u_e^2 \overline{C_1}$ that can be written

$$\frac{\overline{C_1} + \overline{C_2}}{\overline{C_1}} = \frac{\rho \bar{e} u_e^2}{2\sigma}. \tag{4.61}$$

Equation (4.61) shows that the shape of the bell (left-hand term) is a function only of the Weber number (right-hand term). In this limit, the functions $\tilde{F}$ and $\tilde{G}$ can be calculated through the integration of equation (4.41). When this equilibrium is perturbed with a velocity decrease δu_e, the difference of pressure p is no longer zero and the new equilibrium takes the form

$$\overline{C_1} + \overline{C_2} - \frac{p}{2\sigma} = \frac{\rho \bar{e} u_e^2}{\sigma} \overline{C_1} \left(1 - 2\frac{\delta u_e}{u_e}\right). \tag{4.62}$$

Using the equilibrium (4.61), equation (4.62) can be simplified and leads to the expression for the pressure variation:

$$\alpha = \frac{pL}{2\sigma} = 2(\tilde{F} + \tilde{G})\frac{\delta u_e}{u_e}. \tag{4.63}$$

According to equations (4.35) and (4.36), if the Reynolds number is weakly affected by the velocity perturbation, then $\delta u_e/u_e = \delta U_0/U_0$. Using the definition of the characteristic length, we thus get $2\delta u_e/u_e = \delta L/L$ and equation (4.63) can be used to evaluate the characteristic length variation for a critical pressure difference $\alpha^\star$:

$$\frac{\delta L}{L} = \frac{\alpha^\star}{\tilde{F} + \tilde{G}}. \tag{4.64}$$

The curvature function, $\tilde{F} + \tilde{G}$, is presented in figure 29(a). In the range $65° < \psi_0 < 83°$, a good estimation of the function is $(\tilde{F} + \tilde{G}) \simeq 3.6 \pm 10\%$. From figure 28(a), a reasonable value of $\alpha^\star$, for $\psi_0 \in [65°, 83°]$ which was the typical angles range of the
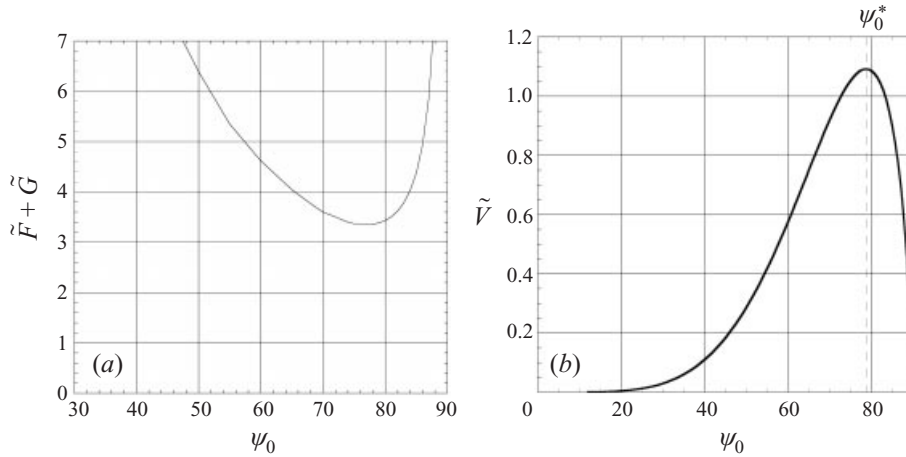
FIGURE 29. (a) Evolution of the curvature function $\frac{1}{2}(\tilde{F} + \tilde{G})$ with the ejection angle ψ_0. (b) Evolution of the bell volume $\tilde{\mathcal{V}}$ with the ejection angle ψ_0 in the limit $\tilde{r}_i \ll 1$ and $\tilde{u}_e = 1$.

data reported in figure 28(b), is $\alpha^\star \approx 0.5$. According to equation (4.64), this leads to the characteristic length variation $\delta L/L \simeq 0.14$, which gives the daughter to mother size ratio $D_{j+1}/D_j \simeq 0.86$. This is in reasonable agreement with the results reported in figure 28(b), where, $D_{j+1}/D_j \simeq 0.82$.

We now concentrate on the limit where the second term in equation (4.54) dominates. Since the instability of the bells leads to their bursting, we discuss this second limit around $\alpha = 0$, where according to figure 26(b) $(\partial \tilde{V}/\partial \alpha)_{\psi_0} = 0$. Assuming that ψ_0 results from the local balance of forces at the point of detachment (see §4.2), one deduces that $\mathrm{d}\psi_0/\mathrm{d}p > 0$ and the stability of the bell, according to equation (4.54), only depends on the sign of $(\partial \tilde{V}/\partial \psi_0)_{\alpha=0}$. To simplify the presentation, we work in the limit $\tilde{r}_i \ll 1$ and $\tilde{u}_e = 1$. In this limit, the volume of the bell $V \equiv \tilde{V}L^3$, can be evaluated using equations (4.41) and (4.42):

$$\tilde{V} = 2\pi \left[\left(1 + \frac{\cos^2(\psi_0)}{2} \right) \cos(\psi_0) \ln \left(\frac{\cos(\psi_0)}{1 - \sin(\psi_0)} \right) - \tfrac{3}{4} \sin(2\psi_0) \right], \qquad (4.65)$$

The evolution of $\tilde{V}(\psi_0)$ described by equation (4.65) is presented in figure 29(b).

This evolution is characterized by the existance of a maximum for $\psi_0^\star = 78.78°$, a solution of the equation $\mathrm{d}\tilde{V}/\mathrm{d}\psi_0 = 0$. That value separates the stable bells ($\psi_0 < \psi_0^\star$) where $(\partial \tilde{V}/\partial \psi_0)_{\alpha=0} > 0$ from the unstable ones ($\psi_0 > \psi_0^\star$) where $(\partial \tilde{V}/\partial \psi_0)_{\alpha=0} < 0$.

In this latter case, the instability leads to the bursting of the bell which keeps $\alpha = 0$ but does not affect the origin of the instability, $\psi_0 > \psi_0^\star$. One thus expects the instability to reproduce itself continuously. This limit corresponds to the instability presented in figure 17. The period T, of the instability is presented in figure 30(a) as a function of the characteristic time L/U_0. This figure suggests a linear relationship $T \approx 19.7D/U_0$, which is of the order of the formation time $T_F(\psi_0 = 87°) = 13L/U_0$.

The instability presented in figure 15 is a little different in the sense that the bell is initially stable, with an angle of ejection $\psi_0 = 75°$. However the upward bulge modifies this angle as it reaches the edge and the whole bell undergoes an unstable cycle. This instability occurs with a well-defined period presented in figure 30(b) as a function of the characteristic time L/U_0. In this case also, the period of the phenomenon is of the order of the formation time.
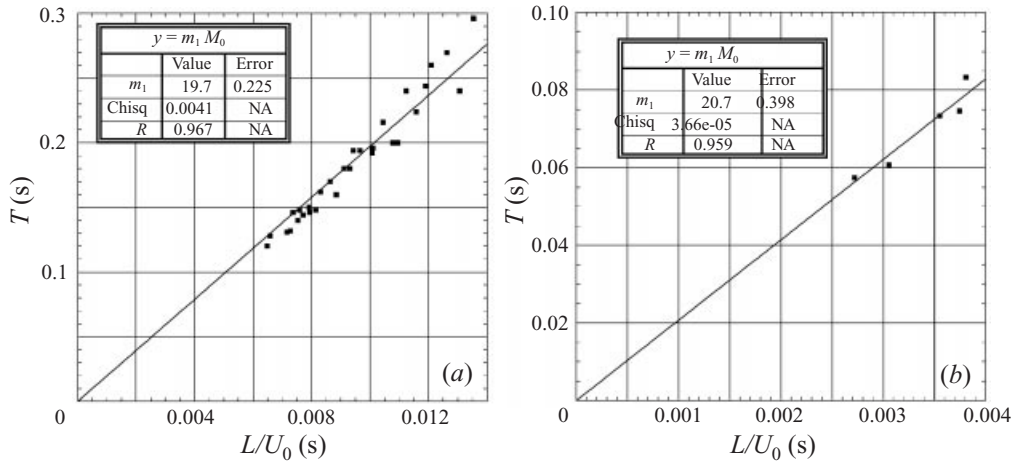
FIGURE 30. Evolution of the period of oscillation: (*a*) pressure forcing, (*b*) liquid film forcing.
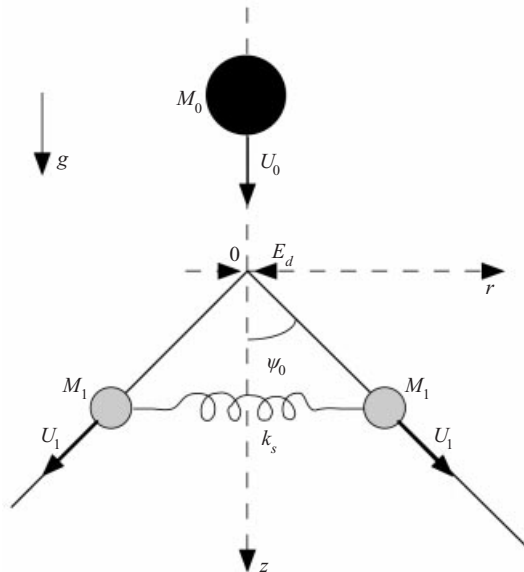

FIGURE 31. Presentation of the particle analogy.

Compared to the ideas presented in Clanet (2000), the present analysis of water bell stability has considered the effect of the jet diameter and thus reveals the existence of a new destabilizing scenario, through the recirculation of a liquid bulge. It also provides a detailed quantitative study of the cascade instability through the discussion of the relation $D_{j+1}(D_j)$. Finally, the study of the pressure effect has confirmed its influence on the stability but also revealed the existence of stable cusps, observed experimentally.

4.6. *A particle analogy*

The particle analogy we propose, in order to complete the physical description of the water bell problem, is presented in figure 31. A mother particle of mass, M_0, and velocity, U_0, is subjected at $t = 0$ to the disintegration energy, $M_0 E_d$, which leads to

twin particles of mass M_1 and velocity U_1, each one forming the angle ψ_0 with the initial direction of the mother.

The conservation of mass after the disintegration is written $M_1 = M_0/2$. It follows that the conservation of momentum, $2M_1 U_1 \cos(\psi_0) = M_0 U_0$, reduces to $U_1 = U_0/\cos(\psi_0)$. Finally, in the limit where the total energy of the particles corresponds to their kinetic energy, energy conservation leads to

$$U_1^2 = U_0^2 + 2E_d. \tag{4.66}$$

Using the result of the momentum conservation, we get the expression for the angle of ejection:

$$\cos(\psi_0) = \frac{1}{\sqrt{1 + 2E_d/U_0^2}}. \tag{4.67}$$

In the limit $2E_d/U_0^2 \ll 1$, where the disintegration energy is weak compared to the initial kinetic energy, the twin particles follow almost the same trajectory as the mother. In the opposite limit $2E_d/U_0^2 \gg 1$, the angle of ejection tends to $\pi/2$. This behaviour of the angle of ejection is close to that observed for ψ_0^{max}.

If we consider the effect of an internal energy per unit of mass, E_{int}, the balance (4.66) is replaced by $U_1^2 = U_0^2 + 2\Delta E$, where $\Delta E \equiv E_d - (E_{int(1)} - E_{int(0)})$. Since the momentum equation is not affected, the expression for the angle is simply:

$$\cos(\psi_0) = \frac{1}{\sqrt{1 + 2\Delta E/U_0^2}}. \tag{4.68}$$

Compared to the previous expression (4.67), the disintegration energy E_d has been replaced by the difference ΔE. It follows that if the internal energy of the twins, $E_{int(1)}$, is larger than the internal energy of the mother, $E_{int(0)}$, then $\Delta E < E_d$, and the angle of ejection is reduced. This behaviour reproduces that of the angle of ejection of the liquid film for moderate Weber numbers, that is when the surface energy cannot be neglected compared to the kinetic energy.

Assuming that after the disintegration, the twin particles are connected by a spring of strength k_s $[M/T^2]$, we look for their trajectory, first in the zero gravity limit, $g = 0$. The momentum evolution equation projected onto r- and z-axes is

$$M_1 \frac{d^2 r_1}{dt^2} = -k_s r_1, \tag{4.69}$$

and

$$M_1 \frac{d^2 z_1}{dt^2} = 0, \tag{4.70}$$

where r_1 and z_1 are the coordinates of a twin. This system leads to the trajectory

$$\frac{r_1}{R} = \tan(\psi_0) \sin\left(\frac{z_1}{R}\right), \tag{4.71}$$

where $R \equiv \sqrt{M_0 U_0^2/(k_s)}$ is the characteristic length of the problem. This trajectory is obtained with the initial condition $(dr_1/dz_1)_0 = \tan(\psi_0)$. Each of the particles has a sine trajectory in the (z, r)-plane and will meet its twin at $z_{max}/R = \pi$. This trajectory is obviously symmetrical about $z_e/R = \pi/2$ and is the equivalent of the catenary solution. The only difference with the water bell problem is that the connecting force does not act normally to the trajectory but always along the radial direction.

The main advantage of this model is to improve the understanding of the effect

of gravity. Indeed, in this particle analogy, gravity changes $z_1 = U_0 t$ (which results from equation (4.70)), into $z_1 = U_0 t + g t^2/2$. Since equation (4.69) remains the same, trajectory of the twins with gravity is described by the equation

$$\frac{r_1}{R} = \tan(\psi_0) \sin\left[\frac{1}{F}\left(\sqrt{1 + 2F\frac{z_1}{R}} - 1\right)\right], \tag{4.72}$$

where $F \equiv gR/U_0^2$ is the reduced gravity. In the limit $F \ll 1$, we recover the sine trajectory (4.71) and in the limit, $F \gg 1$, we recover the ballistic trajectory $z_1 = g r_1^2/(2\tan^2(\psi_0)U_0^2)$.

An evaluation of the symmetry of the trajectory is given by the ratio $SYM \equiv z_{max}/z_e - 2$. When $SYM > 0$, the equatorial plane is closer to the disintegration location than to the connecting point z_{max}, and for $SYM < 0$ the opposite behaviour is observed. At $SYM = 0$, the equatorial location corresponds to half the maximal location z_{max}. Using the trajectory (4.72), we get

$$SYM = \frac{2\pi F}{4 + \pi F}. \tag{4.73}$$

Since $F \geqslant 0$, this expresion is always positive and continuously increases from 0 at $F = 0$ to 2 at $F \gg 1$. The symmetry of the trajectory observed in the limit $g = 0$ is thus broken as soon as gravity is considered.

Physically, the acceleration due to gravity makes the velocity of the particles greater after the equator than before. We first imagine that the trajectory is symmetrical. Then, at the two locations $z_e - c$ and $z_e + c$, where $c \in [0, z_e]$ is a constant, both the radial location r and the radius of curvature R_c are the same. If r is constant, the force of the spring is constant. However, even if R_c is constant, since the velocity is increased by gravity, it follows that the centrifugal acceleration U^2/R_c, is increased. The assumption of symmetry does not satisfy the equality of forces. It follows that the symmetrical shape is not stable and must be replaced by the shape for which, if r is the same, as U increases, R_c decreases so that U^2/R_c remains constant. The radius of curvature at $z_e + c$ is then larger than at $z_e - c$. This implies that the equatorial plane is closer to the disintegration location than to the connecting point z_{max}.

5. Conclusion

This paper is devoted to the water bell problem first investigated by Savart in 1833. Several questions have been addressed concerning the conditions of ejection of the film from the impactor, the ejection angle ψ_0, the shape of the bells, the dynamics of their formation and finally their stability.

Concerning the detachment of the film, we have shown that for a given jet diameter and velocity, it can only occur between two limits: one corresponding to a large diameter ratio $X > 1$ and the other one to $X < 1$. The conditions for detachment at these limits have been experimentally determined and then modelled.

When these conditions are fulfilled, the film leaves the impactor with the angle ψ_0. In the limit $We \gg 1$, this angle depends only on X but for moderate Weber numbers ψ_0 becomes a function of We.

Concerning the bell shape, with no pressure difference between the inside and the outside of the bell we have shown that the catenary first proposed by Boussinesq is a good estimation of the shape, provided one considers the modifications of the flow related to the impactor and takes the correct ejection angle ψ_0 related to these initial conditions.

The study of the dynamics of formation reveals a quasi-constant vertical velocity of the edge of the liquid sheet V_f, and a formation time T_F, strongly dependent on ψ_0.

Finally, we have derived a general stability criterion and shown the sensitivity of the bells to both the pressure difference across the liquid sheet and to the ejection angle from the impacting disc. In this later case, we find a critical angle of ejection above which the bell is periodically destroyed and created. The period of the cycle is shown to scale linearly with the formation time T_F.

It is hoped that this paper will stimulate more analytical work on the time-dependent solution which has been discovered.

REFERENCES

BARK, F. H., WALLIN, H.-P., GALLSTEDT, M. G. & KRISTIANSSON, L. P. 1979 Swirling water bells. In *J. Fluid Mech.* **90**, 625–639.

BECQUEREL, A. C. 1841 Funérailles de M. SAVART. In *Archives de l'Académie des Sciences de Paris*, pp. 1–10.

BENEDETTO, D. & CAGLIOTI, E. 1998 A stationary action principle for the water sheet. *Eur. J. Mech. B/Fluids* **17**, 769–772.

BOND, W. N. 1935 The surface tension of a moving water sheet. *Proc. Phys. Soc.* B **67**, 549–558.

BOUSSINESQ, J. 1869*a* Théories des expériences de Savart, sur la forme que prend une veine liquide après s'être choquée contre un plan circulaire. *C. R. Acad. Sci. Paris* **69**, 45–48.

BOUSSINESQ, J. 1869*b* Théories des expériences de Savart, sur la forme que prend une veine liquide après s'être heurtée contre un plan circulaire (suite). *C. R. Acad. Sci. Paris* **69**, 128–131.

CLANET, C. 2000 Stability of water bells generated by jet impacts on a disk. *Phys. Rev. Lett.* **85**, 5106–5109.

HOPWOOD, F. L. 1952 Water bells. *Proc. Phys. Soc.* B **65**, 2.

HUANG, J. C. P. 1970 The break-up of axisymmetric liquid sheets. *J. Fluid Mech.* **43**, 305–319.

LANCE, G. N. & PERRY, R. L. 1953 Water bells. *Proc. Phys. Soc.* B **66**, 1067.

LANDAU, L. & LIFCHITZ, E. 1971 *Physique Theorique: Mecanique des Fluides*. Mir.

PARLANGE, J. Y. 1967 A theory of water bells. *J. Fluid Mech.* **29**, 361–372.

PLATEAU, J. 1873 *Statique Experimentale et Theorique des Liquides*. Gauthier-Villars et Cie.

RAYLEIGH, LORD 1879 On the instability of jets. *Proc. Lond. Math. Soc.* **10**, 4–13.

SAVART, F. 1833*a* Memoire sur la constitution des veines liquides lancees par des orifices circulaires en mince paroi. *Ann. de Chim.* **53**, 337–386.

SAVART, F. 1833*b* Memoire sur le choc d'une veine liquide lancée contre un plan circulaire. *Ann. de Chim.* **54**, 56–87.

SAVART, F. 1833*c* Suite du Mémoire sur le choc d'une veine liquide lancée contre un plan circulaire. *Ann. de Chim.* **54**, 113–145.

SAVART, F. 1833*d* Memoire sur le choc de deux veines liquides animées de mouvements directement opposés. *Ann. de Chim.* **55**, 257–310.

Squire, H. B. 1953 Investigation of the instability of a moving liquid film. *Brit. J. Appl. Phys.* **4**, 167–169.

Taylor, G. I. 1959 The dynamics of thin sheets of fluid. I Water bells. *Proc. R. Soc. Lond.* A **253**, 289–295.

Watson, E. J. 1964 The radial spread of a liquid jet over a horizontal plane. *J. Fluid Mech.* **20**, 481–499.